

# Ohmic n-contacts to Gallium Nitride Light Emitting Diodes

**Jonathan Aguilar**

Physics, Harvard University

*NNIN REU Site: Nanotech—The UCSB Nanofabrication Facility, University of California, Santa Barbara*

*NNIN REU Principal Investigator: Prof. Stephen P. DenBaars, Materials Department, University of California, Santa Barbara*

*NNIN REU Mentor: Kenneth J. Vampola, Materials Department, University of California, Santa Barbara*

*Contact: jaguilar@fas.harvard.edu, denbaars@engineering.ucsb.edu, kvampola@enr.ucsb.edu*

## Abstract:

Efficient light emitting diodes (LEDs) seek to minimize input power while maximizing optical output power. To minimize input power, the total voltage drop across the LED should be reduced. Significant loss occurs at metal-semiconductor junctions where electrical contact is made to the diode. This experiment studied different methods of minimizing the voltage drop across the LED. The p-contact on our device is made of indium tin oxide (ITO), which cannot tolerate annealing temperatures of 650°C or more [1,2]. The titanium aluminum gold (Ti/Al/Au) triple layers we use have been demonstrated to be effective n-contacts, but require annealing temperatures upwards of 750°C [3]. Therefore, our Ti/Al/Au contacts have been left unannealed, resulting in Schottky diode-like behavior of the junction.

## Experimental Procedure

To improve the quality of the contact behavior, two contact schemes and methods of treating the n-type gallium nitride (GaN) surface were tested. The Ti/Al/Au scheme was compared to a copper germanide (Cu<sub>3</sub>Ge) scheme. Cu<sub>3</sub>Ge contacts to n-GaN can be annealed at temperatures within the tolerance of ITO [4]. Hydrogen chloride (HCl)-based wet etches are effective at removing native gallium oxides (Ga<sub>x</sub>O<sub>y</sub>) [5]. Lastly, etching the n-GaN surface by reactive ion etching (RIE) has been demonstrated to both improve ohmic behavior of the contact and decrease contact resistance [6]. The effect of annealing temperature on the Cu<sub>3</sub>Ge contact scheme was also examined, but is not presented here.

Ohmic behavior and contact resistance were determined using the transmission line method (TLM). We used quarters of 2-inch Al<sub>2</sub>O<sub>3</sub> wafers with epitaxial LED layers grown by metal-organic chemical vapor deposition (MOCVD). Before processing, the n-type GaN layer was exposed using an inductively coupled plasma etch to simulate etch damage that occurs during regular LED processing.

Sample	n-GaN treatment	Contact Scheme	Annealing Conditions
A	HCl	Ti/Al/Au	Unannealed
B	HCl	Cu <sub>3</sub> Ge	550°C
C	RIE, 110W	Cu <sub>3</sub> Ge	550°C
D	RIE, 170W	Cu <sub>3</sub> Ge	550°C

Table 1: Contact scheme and surface treatment combinations.

## Contact Deposition

Contact schemes and surface treatments were distributed across samples according to Table 1. Contact metals were deposited by electron-beam evaporation. Ti/Al/Au layer thicknesses were 200/600/3000Å. The Cu<sub>3</sub>Ge contact scheme was deposited as Ge/Cu/Ge:400/970/400Å. This 30 at.% Ge composition has been observed to yield the low-resistivity ε<sub>1</sub>-Cu<sub>3</sub>Ge phase after annealing [7]. Cu<sub>3</sub>Ge annealing was performed in a rapid thermal annealer at 550°C for 10 minutes in N<sub>2</sub> with a flow rate of 5 sccm. Ti/Au (200/3000Å) contact pads were then deposited on top of all n-contacts. The final step was to isolate the TLM patterns by etching around them through the n-type GaN to the Al<sub>2</sub>O<sub>3</sub> substrate. The width of the resulting structure was 100 μm and the depth was 3.6 μm. Contact dimensions were 94 × 50 μm<sup>2</sup>, and the TLM spacings varied from 5 μm to 40 μm.

## Surface Treatment

n-GaN HCl immersion and RIE treatment were examined for their effect on ohmic behavior and contact resistance. Because these treatments affect only the n-GaN and not the contact, the resultant relative improvements in electrical performance are expected to be independent of the particular contact scheme. Therefore, these surface treatments were only tested on the Cu<sub>3</sub>Ge contact scheme. HCl treatment was performed by immersion in a HCl:DI 1:3 solution for 1 minute at room temperature. RIE dry etch was performed in SiCl<sub>4</sub> with a flow rate 10 sccm. Chamber pressure was 25 mTorr, and the etch depth was 50 nm into the n-type GaN. The samples were not temperature controlled during the RIE etch.

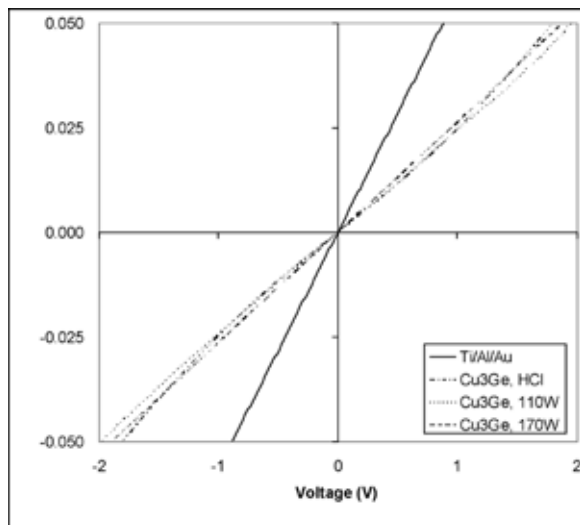


Figure 1: Current-voltage characteristics for different  $\text{Cu}_3\text{Ge}$  contacts on n-GaN.

## Surface Treatment and Contact Scheme Results and Discussion

As can be seen in Figure 1, the behavior of Samples A and D were closest to ohmic. There are several possible explanations for ohmic behavior in samples. One is the removal of surface oxides and other types of surface scum that tend to accumulate during LED processing. In the case of the Sample A, the removal of gallium oxide by HCl etching is believed to be responsible for forming an ohmic contact. However, HCl immersion alone did not produce ohmic behavior in the  $\text{Cu}_3\text{Ge}$ -based samples. The emergence of ohmic behavior only after RIE treatment indicates other mechanisms besides oxide removal.

Schuette and Lu present evidence that RIE creates both Ga and N vacancies, but Ge preferentially diffuses into N vacancies and behaves as a donor, increasing the level of n-doping of the GaN [6].  $\text{SiCl}_4$  may also decrease the length of the electron depletion region [4]. Another possibility is that the RIE treatment helps remove etch damage caused by previous etching.

Figure 2 compares the contact resistances of the samples. The contact resistance of unannealed Ti/Al/Au was calculated to be  $\sim 1.8 \cdot 10^{-4}$ , less than half that of  $\text{Cu}_3\text{Ge}$  when both samples are treated only with HCl. However, it can be seen that RIE treatment dramatically reduced the contact resistance of the  $\text{Cu}_3\text{Ge}$  contacts.

## Conclusions

Schuette and Lu show that RIE treatment reduces the length of the depletion zone in n-GaN [4]. Thus, the relative improvement of the  $\text{Cu}_3\text{Ge}$  contact with RIE surface treatment should be true regardless of contact scheme. Ti/Al/Au contacts will be used for further experimentation with RIE because of their superior performance compared to  $\text{Cu}_3\text{Ge}$  in the HCl control test. Lastly, the data indicate that there is a need to optimize RIE etching power for ohmic behavior and low contact resistance.

## Acknowledgments

Thanks to Ken Vampola, Prof. Stephen DenBaars, and the rest of the SSLDC. I would also like to thank Seoul Semiconductor for supporting this work, and Angela Berenstein, the NSF, and the NNIN REU Program for the opportunity to work at UCSB.

## References

- [1] Determined during previous laboratory testing.
- [2] Jang and Song. J. Appl. Phys. 101 (2007).
- [3] Wang et. al. J. Appl. Phys. 89 (2001.)
- [4] Schuette and Lu. J. Appl. Phys. 101 (2007).
- [5] Ren et. al. J. Electrochem. Soc. 14 (1997).
- [6] Schuette and Lu, J. Vac. Sci. Technol. B 23 (2005).
- [7] Aboelfotoh et. al., J. Appl. Phys. 76 (1994).

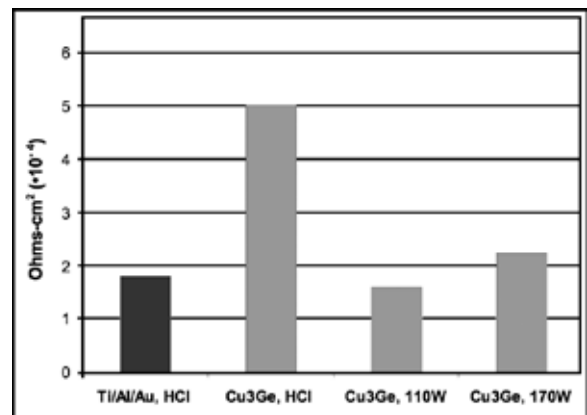


Figure 2: Specific contact resistance for different treatments.

# Photoelectrochemical Etching of Silicon Carbide

**Henry David Babb III**

Electrical Engineering, Prairie View Agricultural & Mechanical University

*NNIN REU Site: Howard Nanoscale Science & Engineering Facility (HNSEF), Howard University*

*NNIN REU Principal Investigator: Dr. Gary L. Harris, Director, HNSEF, Howard University*

*NNIN REU Mentor: Mr. James Griffin, Howard Nanoscale Science & Engineering, Howard University*

*Contact: babbtre@yahoo.com, gharris@msrce.howard.edu, griffin@msrce.howard.edu*

## Abstract

Silicon carbide (SiC) was etched by photoelectrochemical (PEC) in a dilute solution of hydrofluoric acid (HF). PEC etch masks were formed on SiC by sputtering 10 nm of titanium and evaporating 150 nm of platinum and heating the contacts to 600°C by rapid thermal annealing. PEC etching was performed with a UV light power density of 125 mW/cm<sup>2</sup> and a current density 0.992 mA/cm<sup>2</sup>. Etching was performed for one hour at room temperature. The SiC nanopores were then oxidized at 1150°C for four hours to form SiO<sub>2</sub> and subsequently placed in an HF solution to remove the oxide.

## Introduction

SiC is so chemically resistive that only a few techniques are available to etch it. Hot potassium hydroxide (KOH) will etch SiC, however KOH will also remove almost all etch masks. Reactive ion etching (RIE) can be used to etch SiC also and a suitable etch mask exists for this process. RIE has very high anisotropy and good morphology, but it's an expensive process with no dopant selectivity. It does have a low etch rate but depending on the application, this can be considered an advantage or disadvantage. Photoelectrochemical etching has a more controlled etch rate from low to very high. It yields good morphology on 6H-SiC and excellent dopant selectivity. It's relatively inexpensive when compared to RIE, but only has fair morphology on 3C-SiC [1].

Photoelectrochemical etching is the process of using ultraviolet light, voltage, and chemicals to etch materials such as silicon carbide and gallium nitride. Pure silicon carbide is not a good conductor of electricity so its essential that silicon carbide be n-doped meaning more electrons are present than holes. Through photoelectrochemical etching, holes are generated with ultraviolet light by breaking some of the bonds in the SiC (Figure 1).

Voltage is applied to the sample forcing holes to the surface of the sample to facilitate etching by hydrofluoric acid.

## Experimental Procedure

First we characterized titanium/platinum (Ti/Pt) contacts on SiC as an etch mask by sputtering 10 nm of Ti and evaporating 150 nm of Pt and heating the contacts to 600°C by rapid thermal annealing. The process of annealing makes sure that the Ti/Pt mask fully adheres to the surface of the SiC sample. SiC nanopores are formed on the substrate surface by PEC. PEC conditions for nanopore formation were: UV light power density of 125 mW/cm<sup>2</sup> and a electrical current density of 0.992 mA/cm<sup>2</sup> in a dilute solution of HF. Etching was performed for one hour for both 3C and 6H SiC. Nanopore formation was followed by oxidation of the SiC nanopores in a wet oxidation furnace for 4 hours at 1150°C which changes the SiC nanopores to SiO<sub>2</sub>. Finally a chemical etch of the newly formed SiO<sub>2</sub> was performed in HF.

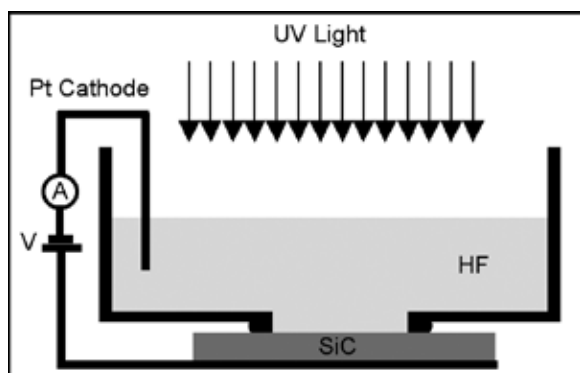


Figure 1: Photoelectrochemical setup.

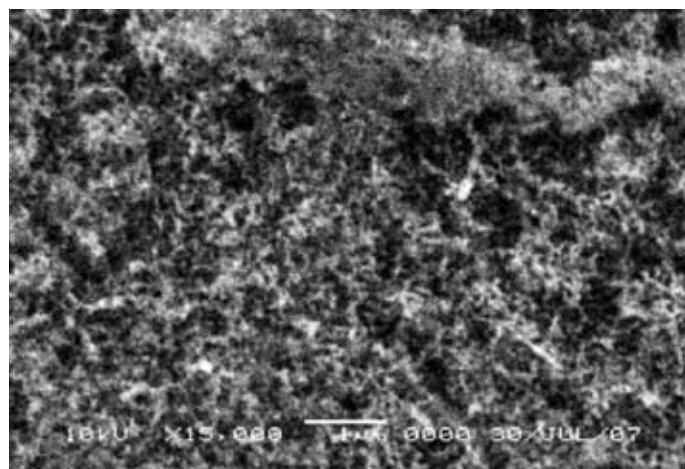


Figure 2: Porous silicon carbide.

## Results

We produced nanopores on the surface of the SiC through PEC as seen in Figure 2. After oxidation, we could tell from the surface of the SiC sample that SiO<sub>2</sub> had formed because of the blue color that was visible on the sample where the nanopores were. SiO<sub>2</sub> was then removed with HF. We obtained etch depths of 13 μm for the 3C-SiC and 4.6 μm for 6H-SiC. Since 3C has a less dense lattice, we were able to obtain higher etch rates. Figure 3 is an SEM image of a 6H-SiC PEC etched sample.

## Conclusion/Future Work

In conclusion, we were successful in forming nanopores, oxidizing the nanopores to form SiO<sub>2</sub>, and removing the SiO<sub>2</sub> to get a clean etched surface on SiC. However we did have issues with getting the Ti/Pt mask to fully adhere to the SiC surface. We were able to solve this issue by heating the sample at 600°C. Some samples were not etched because they were either undoped or low doped. In the future it would be beneficial to establish etch rates on 3C, 4H and 6H SiC based on doping concentration.

## Acknowledgements

I would like to thank Dr. Gary L. Harris, Mr. James Griffin, Dr. Peizhen Zhou, the staff and students at HNF. I would also like to thank the National Nanotechnology Infrastructure Network Research Experience for Undergraduates Program and the National Science Foundation for funding.

## References

- [1] "Properties of Silicon Carbide" Edited by Gary L. Harris, EMIS Datareviews Series No. 13, INSPEC, the Institution of Electrical Engineers 1995.
- [2] Hossain, T., Khan, F., Adesida, I., Bohn, P., and Rittenhouse, T. "Nanoporous Silicon Carbide for Nanoelectromechanical Systems Applications" NASA/CR 2003.
- [3] Streetman, B.G. and Banerjee, S.K. "Solid State Electronic Devices" Pearson Prentice Hall 2006.
- [4] Shishkin, Y., Choyke, W.J., and Devaty, R.P. "Photoelectrochemical Etching of n-type 4H SiC" 2004 J.Appl.Phys. 96, 2311.

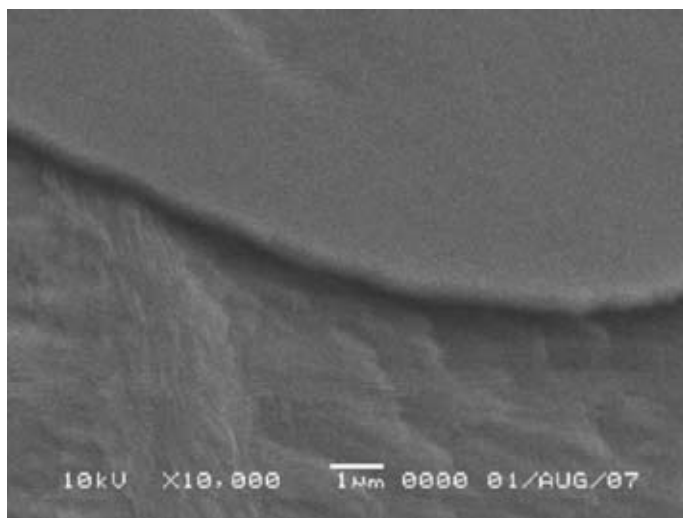


Figure 3: 6H-SiC after PEC etch.

# Self-Assembly and Optical Characterization of Semiconductor and Metallic Nanocrystal Monolayers and Multilayers

**Robert Bradley**

Chemical and Biomolecular Engineering, North Carolina State University

*NNIN REU Site: Nanoscience at the University of New Mexico*

*NNIN REU Principal Investigator: Prof. C. Jeffrey Brinker, Chemical and Nuclear Engineering, University of New Mexico, Sandia National Laboratories*

*NNIN REU Mentor: Shisheng Xiong, Center for High Technology Materials, Advanced Materials Laboratory, University of New Mexico*

Contact: [robradle@ncsu.edu](mailto:robradle@ncsu.edu), [cjbrink@sandia.gov](mailto:cjbrink@sandia.gov), [ssxiong@unm.edu](mailto:ssxiong@unm.edu)

## Abstract

Interactions between semiconductor and metallic nanocrystals are the subject of intensive investigations. Enhanced photoluminescence (PL) yield of quantum dots in the presence of notable nanoparticles or nanohole arrays has potential applications in light-emitting diodes (LED) and sensors. Surface plasmon resonances (SPR) are believed to either increase the PL efficiency by enhancing the local exciting field or cause nonradiative damping due to energy transfer through an inverse route.

## Introduction

We studied the collective interactions, in terms of linear and nonlinear optical properties, between cadmium selenide (CdSe) quantum dots, rods, cadmium telluride (CdTe) tetrapods and gold (Au) nanoparticles (NPs), comprised in monolayers and multilayers. Ultra thin films that incorporated NPs with a size of several nanometers were successfully created via an interfacial evaporation induced self-assembly (EISA) process. These films assembled on the surface of water within a polymethylmethacrylate (PMMA) polymer matrix and were then transferred to desired substrates. Similarly, ultra thin films of pure PMMA were assembled, acting as a dielectric spacer between the two parallel layers of semiconductor and metallic NPs. Atomic layer deposition (ALD) was also utilized, allowing us to achieve precise control on the thickness of spacing layers. Finally, patterning of PMMA supported nanocrystal monolayer thin films was demonstrated. Our results indicate that the PL is affected by the distance between the semiconductor and Au nanoparticles.

## Fabrication of Thin Films

Solutions of PMMA, CdSe nanocrystals or quantum dots, and Au nanocrystals, in an appropriate ratio, were dissolved in toluene. One drop of the solution was carefully released over a deionized water surface sitting in a Petri dish. The suspension of nanocrystals spread out over the surface and a thin film formed through interfacial evaporation-induced self-assembly as shown in Figure 1. The thin films consisted of the nanoparticles embedded in the PMMA polymer matrix. After the toluene evaporated, the thin film was captured on a substrate of our choice by submerging the substrate and bringing it up through the thin film. The sample was then left to dry undisturbed. The weight fraction of CdSe to Au nanocrystals within the solution was varied to explore the effect on photoluminescence. We also prepared multilayer thin films of the ratio-varied solutions to explore how stacking the layers would affect the PL.

First, we attempted to fabricate a binary nanocrystal superlattice from CdSe and Au nanocrystals dispersed with PMMA in toluene and let them co-assemble on the interfacial surface. However, the

transmission electron microscopy (TEM) image in Figure 2 clearly indicates that isolated islands of nanocrystals with severe overlapping formed instead of a homogeneous monolayer thin film. Nevertheless, significant PL quenching was observed due to appropinquity of the two different types of nanocrystals when compared to the PL readings from a solution and monolayer thin film comprised solely of CdSe quantum dots.

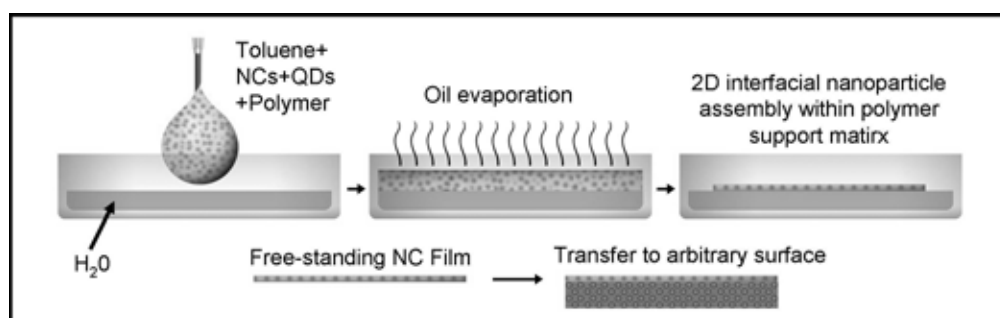


Figure 1: Schematic detailing evaporation induced self-assembly (EISA).

A) Solution dropped onto surface, B) Oil evaporation, C) 2D interfacial nanoparticle assembly within polymer support matrix, D) Free-standing thin film, and E) Transfer to arbitrary surface.

Believing that the close proximity of the Au nanocrystals to the CdSe nanocrystals caused the quenching effect, we redesigned our experiment to further distance the two NPs by placing a dielectric spacing layer between a thin film composed of Au NPs and another thin film of CdSe NPs. In addition, this new strategy allowed us to tune the width of the spacing layer and this distance became the independent variable in our experiments.

### Thin Films with Dielectric Spacing Layer

One thin film, composed of Au NPs, was transferred onto a glass substrate. Figure 3 shows how the solution composed solely of Au nanocrystals and PMMA creates a monolayer thin film, where the Au NPs do not coagulate, but spread out into a thin even film. Thin films composed solely of PMMA polymer were then captured on top of the Au nanocrystal layer until the desired thickness was obtained. Finally, the last thin film layer composed of CdSe NPs and PMMA was captured on top of all the other thin films. As the thin film layers were added to the sample, the surface of the sample became increasingly uneven. When the surfaces of the samples were scanned with a laser, the photoluminescence readings had no correlation to the number of PMMA spacing layers.

Seeking to better control the thickness and quality of the dielectric spacing layer, we utilized atomic layer deposition (ALD) to deposit a layer of amorphous  $\text{SiO}_2$ . We prepared 15 samples of  $2 \text{ cm}^2$  silicon wafer chips by capturing a single Au ultra thin film layer on each wafer through EISA. The samples were then plasma-etched in order to render the surface hydrophilic and placed within the ALD instrument. All samples, heated to  $50^\circ\text{C}$ , were exposed to alternating cycles of vaporized  $\text{SiCl}_4$  and  $\text{H}_2\text{O}$  in order to build up a dielectric spacing layer. One sample was removed from the instrument after every 30 cycles of deposition. A final thin film layer of CdSe and PMMA was captured on top of the amorphous  $\text{SiO}_2$  to form a sandwich structure.

Electron beam lithographic patterning of Au and PMMA monolayer thin films has also been demonstrated. As a positive photoresist, PMMA can be washed away in the developer when exposed to light. Figure 4 shows an optical microscopy image of a patterned thin film. The diameter of the wheel is approximately  $40 \mu\text{m}$  and the width of the lines is about  $1 \mu\text{m}$ . Our patterning of these thin films suggests the ability to use interfacial assembly in device fabrication.

### Results

We were able to successfully use interfacial assembly to create mono and multilayer thin films that incorporated semiconductor and noble nanocrystals. We also explored novel methods to create spacing layers between the two parallel thin films of CdSe and Au nanocrystals. Our results indicate that the photoluminescence of semiconductor nanocrystals can be affected by the proximity of noble metallic nanocrystals.

### Acknowledgments

I would like to sincerely thank Professor Jeff Brinker and my mentor, Shisheng Xiong, for their guidance and support. Special thanks are also extended to the Brinker and Boyle Groups, the UNM coordinators, the National Science Foundation, and the National Nanotechnology Infrastructure Network Research Experience for Undergraduates Program.

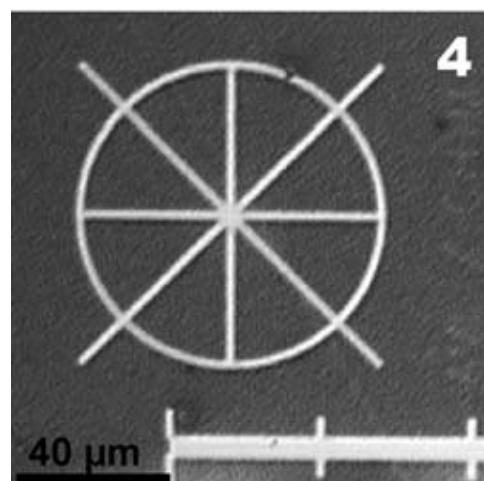
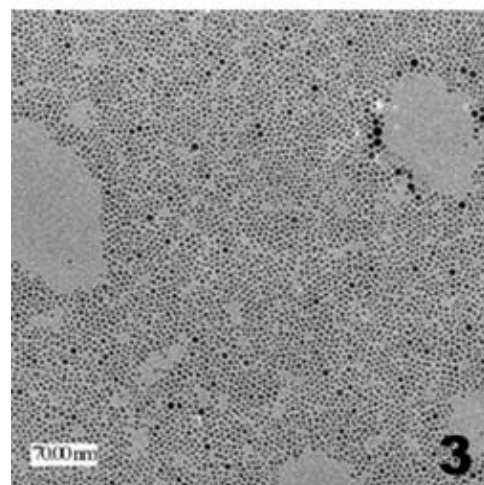
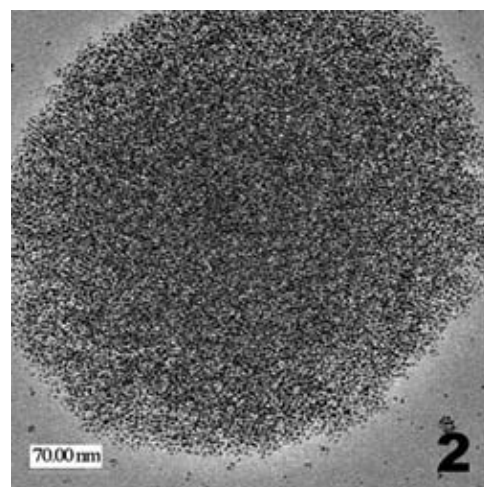


Figure 2, top: TEM image of CdSe / Au NP thin film supported by a PMMA polymer matrix.

Figure 3, middle: Ultra thin monolayer of Au NPs supported by PMMA polymer matrix.

Figure 4, bottom: Optical microscope image of patterned Au monolayer thin film.

# Synthesis, Characterization, and Testing of Polyurethane Nanocomposites

Alla Epshteyn

Chemical Engineering, Tufts University

NNIN REU Site: Michigan Nanofabrication Facility, The University of Michigan Ann Arbor

NNIN REU Principal Investigator: Dr. Ellen Arruda, Mechanical Engineering, University of Michigan

NNIN REU Mentor: Amit Kaushik, Mechanical Engineering, University of Michigan

Contact: [alla.epshteyn@tufts.edu](mailto:alla.epshteyn@tufts.edu), [arruda@umich.edu](mailto:arruda@umich.edu), [akaushik@umich.edu](mailto:akaushik@umich.edu)

## Abstract

The dispersion of nanoscale reinforcements has been shown to raise the strength and stiffness of polymers [1]. In this project, polyurethane (PU) was reinforced with nanometer-sized clay platelets to make nanocomposites through the layer by layer (LBL) assembly process. Samples with 0, 12, 20 and 45 wt% clay were synthesized. Thermal characterization of these samples was done using a differential scanning calorimeter (DSC). Scanning electron microscopy (SEM) was used to measure the thickness, and thermo-gravimetric analysis (TGA) was used to determine the clay content in nanocomposites. Tensile tests at a constant strain rate were performed on a series of nanocomposite samples with an in-house built tensiometer. The nanocomposites were observed to exhibit enhanced mechanical stiffness, yield strength and toughness at various weight fractions of clay.

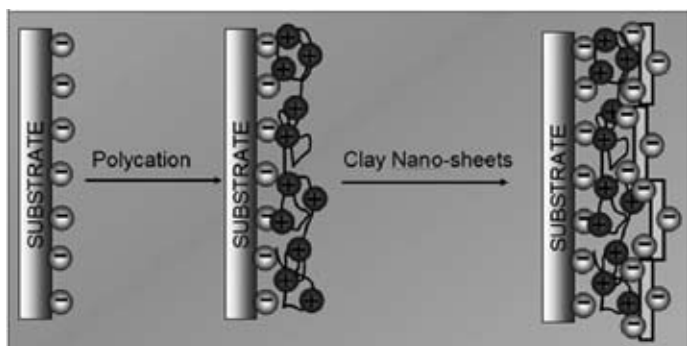


Figure 1: Adhesion of oppositely charged layers.

## Synthesis (Layer by Layer Assembly)

The nanocomposites were synthesized by an emerging method of nanotechnology, the LBL assembly process. LBL is based on sequential deposition of nanometer-thick layers of oppositely charged components to build a multilayered structure. In this preparation, a glass substrate was alternately immersed into solutions of clay nanoparticles and cationic polyurethane, forming a new layer with each immersion through absorption. The oppositely charged layers adhered to each other resulting in homogeneously multilayered thin films on both sides of the glass substrate (Figure 1). These films were then separated from the substrate with a hydrogen fluoride solution. Finally, the films were treated with isopropanol alcohol.

## Characterization

Clay content in each sample was determined with a Perkin-Elmer TGA. A small amount of sample (0.1-0.3 mg) was placed in a weighing pan of the instrument's ultra-sensitive balance and the sample was heated from 50°C to 1000°C at a heating rate of 10°C/min while being purged with air at 20 ml/min. The weight change of each sample was recorded as a function of temperature and the results were compared to pure clay. Given that the inorganic clay has much greater decomposition temperature than the organic polymer, the content of the clay inside the samples was estimated from the comparison of curves. Thermal characterization of the films was accomplished using a Perkin-Elmer DSC machine. A small amount of the sample (3-7 mg) was encapsulated in an aluminum pan and was heat treated from 30°C to 400°C at

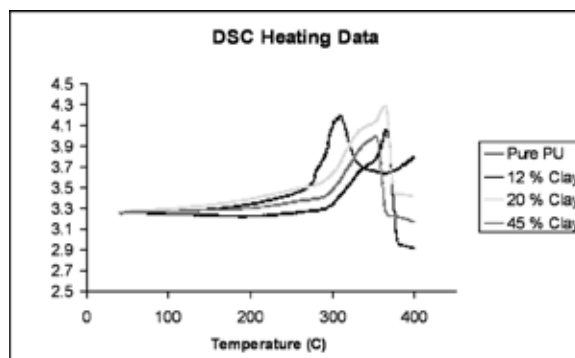


Figure 2: Thermal characterization data via DSC.

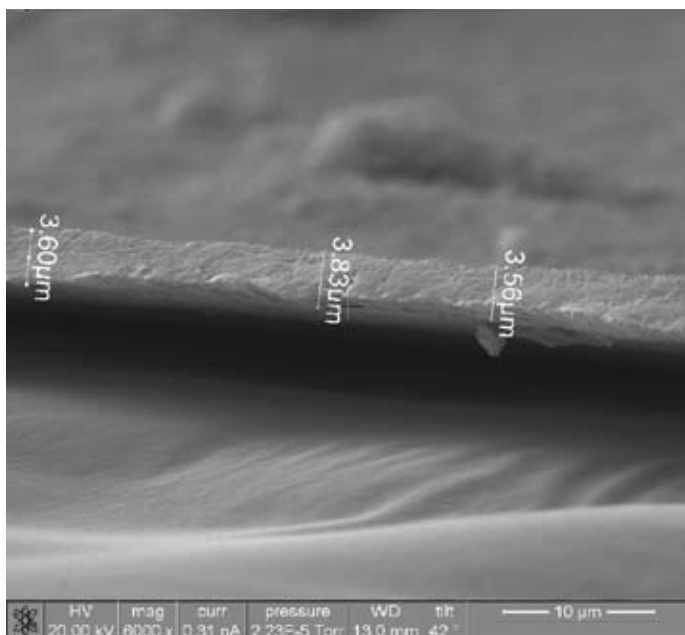


Figure 3: SEM of the 45% clay nanocomposite sample thickness.

10°C/min. The heat flow (W/g) was recorded as a function of sample temperature in order to analyze the results (Figure 3). The thickness of the nanocomposite film samples was measured via SEM to obtain the cross sectional area for stress calculations (Figure 3). The nanocomposites were gold sputtered prior to observation via SEM due to the nonconductive nature of the specimens.

### Testing Methodology

Tensile testing was performed using an in-house designed tensiometer composed of a digital video camera focused on an inverted microscope (see [2] for details). Ultraspheres with a diameter of 25  $\mu\text{m}$  were arranged on the specimen surface. The axial servomotors were controlled using LabVIEW software, which also synchronized data acquisition from the load element with image acquisition from the digital camera. The samples were loaded at a constant true strain rate of 0.005/s until the sample failed and LabVIEW recorded the corresponding force values and images. The load values were converted to stress and the strain was calculated using Metamorph software by tracking the distance between two ultraspheres. Nominal stress vs. nominal strain graphs were formed, the initial slope of which determined the modulus.

### Results

A transition from ductile to brittle behavior was observed as the clay content increased. The addition of clay to the matrix of PU polymer increased the modulus and the yield strength significantly (Figure 4). When clay was dispersed into the PU with only 12% content, the modulus increased by 11 times and the yield strength increased by 7 times. The ultimate strain of the nanocomposite

with 12% clay content was measured to be about 1/7 of the pure PU strain. The DSC data showed that the peaks of the nanocomposites were all shifted about 50°C. The area under the curves of the DSC data decreased with the clay content increase (Figure 2B).

### Conclusions and Future Work

A number of mechanical properties can be controlled with the change of clay content in the nanocomposite. As clay content increases: strength and modulus increases, while the strain (ductility) decreases. The decrease of the area under the DSC data curve also showed that the polymer becomes constrained by the clay particles. We also found that treating samples with isopropanol increased ductility of the nanocomposites. More samples should be synthesized and tested with 0% to 20% clay content to find the toughest nanocomposite of this family. Altering the polymer used in the nanocomposites could be another project. Finally, when the toughest nanocomposite is found, further characterization could be done by performing fracture tests and high strain rate tests.

### Acknowledgements

The author would like to thank Ellen Arruda, Amit Kaushik, Nicholas Kotov, Paul Podsiadlo, Benjamin Pumplin, Kristen Goble, Anthony Waas, and Yaning Li for their guidance and support. Special thanks are also extended to the National Nanotechnology Infrastructure Network Research Experience for Undergraduates Program, NSF and ONR for sponsoring this internship, as well as to Sandrine Martin and Deborah Swartz for helping the program run successfully.

### References

- [1] Podsiadlo, P., Kaushik, A.K., Arruda, E.M., Waas, A.M., Shim, B.S., Xu, J., Nandivada, H., Pumplin, B.G., Lahann, J., Ramamoorthy, A. and Kotov, N.A., "Ultrastrong and Stiff Polymer Nanocomposites," to appear in Science.
- [2] Calve, S., Mechanical and Morphological Characterization of Self-Assembling Tendons and Myotendinous Junctions *In Vitro*," PhD Thesis, University of Michigan, 2006.

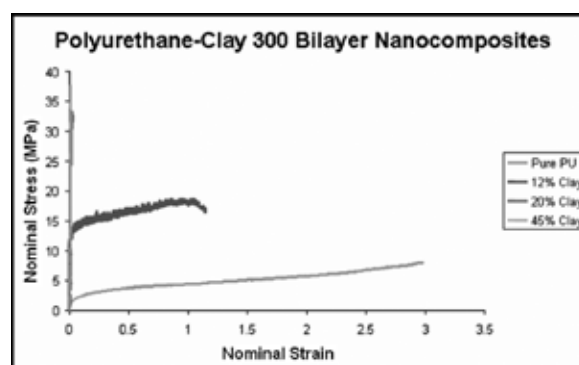


Figure 4: Nominal stress vs. nominal strain data for all nanocomposite samples tested.

## Deterministic Growth of Silicon Nanowires

**Jonathan Ligda**

Physics, Shippensburg University

*NNIN REU Site: Penn State Center for Nanotechnology Education and Utilization, The Pennsylvania State University*

*NNIN REU Principal Investigator: Dr. Suzanne Mohney, Materials Science and Engr., The Pennsylvania State University*

*NNIN REU Mentor: Chad Eichfeld, Department of Materials Science and Engineering, The Pennsylvania State University*

*Contact: jl3281@ship.edu, sem2@psu.edu, cme133@psu.edu*

### Abstract

If it were possible to grow nanowires exactly where needed, then devices could be fabricated with fewer processing steps. We are developing a method that enables silicon nanowires to be grown from the  $\langle 111 \rangle$  sidewalls of trenches etched into silicon wafers. The nanowires are grown from a gold catalyst that is selectively plated on n-type wells patterned into the  $\langle 111 \rangle$  sidewalls of the trenches. The goal of this summer project is to develop a process to fabricate these platforms for nanowire growth using the Penn State Nanofabrication laboratory.

Normally, nanowire growth and alignment for devices involves two separate steps, growth and then alignment. These devices' creation relies on where, and how accurately, the wires are aligned. Being able to determine where the wires are grown by creating areas for gold plating eliminates the two step process of growing and aligning.

### Experimental Procedure

This process starts with  $\langle 110 \rangle$  face silicon wafers with 380 nm of silicon dioxide ( $\text{SiO}_2$ ) grown on the surface. After the oxide growth, we performed electron beam lithography on the samples. ZEP520A resist was spun on, and once applied it was  $\sim 400$  nm thick. The electron beam patterned 200 nm lines running perpendicular to the  $\langle 111 \rangle$  flat in the center of the wafer. After creating these lines, the samples were dry etched using reactive ion etching (RIE) to remove the  $\text{SiO}_2$  layer exposed by the lines. Since the resist layer was very thin compared to the  $\text{SiO}_2$  layer, an etch recipe selective to  $\text{SiO}_2$  was created. Varying gas concentrations and bias voltages, the following recipe gave the best results; 50 sccm  $\text{CF}_4$ , 40 sccm Ar, 8 sccm  $\text{H}_2$ , 300 V DC, and an etch time of 20.5 min.

Being able to grow the wires hinges on having the n-type regions in the silicon. Therefore, applying the dopant so it fills the channels is crucial to the process. The best way to accomplish this was by incorporating spinning and vacuum techniques.

The dopant was in the form of a spin-on-glass with 10% phosphorous included. The spin-on dopant was applied at 1000-2000 rpm, allowing it to coat evenly, and placed in a vacuum chamber allowing any air to escape so the dopant could fill in the channels. The sample was then bake at  $100^\circ\text{C}$  for 30 sec and at  $200^\circ\text{C}$  for 5.5 min to remove solvents. Figure 1 shows an etch channel in  $\text{SiO}_2$  that is filled with dopant.

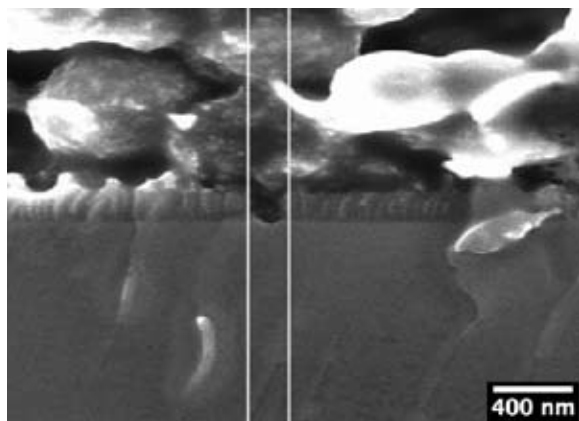


Figure 1:  $\text{SiO}_2$  channel filled with dopant.

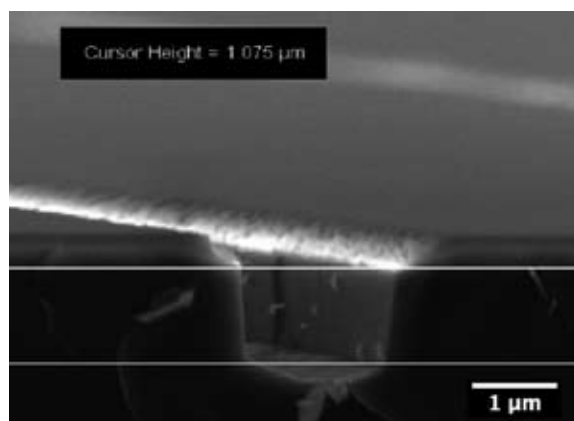


Figure 2: Two minute KOH etched trench.

Diffusing this dopant creates the n-type regions in the silicon needed during subsequent gold plating. A junction depth of 200 nm is desired. After calculations, placing the sample into a furnace for 0.5 hr at 950°C achieved this depth. Placing the sample in a 6:1 ratio of buffered oxide etch (BOE) removed the oxide layer after diffusion.

A masking layer during the future KOH etch was a necessity, and silicon nitride worked adequately. A plasma enhanced chemical vapor deposition system (PECVD) deposited 125 nm of  $\text{Si}_3\text{N}_4$  onto the silicon surface. Samples now went through the photolithography process, using Shipley 1827 photoresist. Lines were patterned 100 nm wide, running parallel with the flat of the wafer. The photoresist was now very thick compared to the nitride, so selectivity was not a very big issue and the etch recipe used for  $\text{SiO}_2$  worked very well. That recipe gave a nitride etch rate of about 60 nm/min, so the etch time was decreased to 3 min.

Etching silicon with KOH at 60°C is slow enough (11 nm/sec) to give a shallow enough trench in a reasonable time (1.5 min). There was now a grid in the middle of the wafer, formed from the n-type regions and the newly etched trenches in the silicon, exposing the areas where the plating of gold occurs. Figure 2 shows a trench etched for 2 min in 60°C KOH bath. The gold plating was on the n-type wells on the sidewalls.

There is a process which causes gold to selectively plate more densely onto these n-type regions [1]. These gold pads were the catalyst used for the nanowire growth step. The nanowires were grown using the vapor-liquid-solid growth mechanism with silane as the silicon precursor gas.

## Conclusions

After growing the wires, scanning electron microscope (SEM) micrographs showed that wires were growing all over the surface. This was because the nitride layer which was supposed to serve as a mask during the gold plating, was no longer on

the surface. We found that the gold had plated on the n-type regions—not only in the trenches, but on the top of the sample as well. Figure 3 shows an image of the n-type regions with wires growing off the surface. The nitride layer disappeared because the sample was placed in a 10:1 BOE for 2 sec. This short immersion completely removed the nitride layer and left the entire surface exposed. The nitride layer possibly had a large amount of hydrogen incorporated, making it etch aggressively in BOE. Even though the image does not show wires growing from the sidewalls, there is no reason not to believe wires were growing there as well.

## Future Work

Future work entails developing a more durable nitride layer so the BOE dip does not strip it off. Also, we need to improve the rinsing techniques after plating the gold so no gold settles onto the surface that is not n-type.

## Acknowledgements

Thanks to the National Science Foundation, the National Nanotechnology Infrastructure Network Research Experience for Undergraduates Program, and The Pennsylvania State University for their funding and facilities. Also, thanks to Dr. Suzanne Mohny, Chad Eichfeld, and the staff at The Pennsylvania State University Nanofabrication Facility for their guidance and advice.

## References

- [1] “Selective plating for junction delineation in silicon nanowires,” C. M. Eichfeld, C. Wood, B. Liu, S. M. Eichfeld, J. M. Redwing, and S. E. Mohny, *Nano Lett.*, in press.

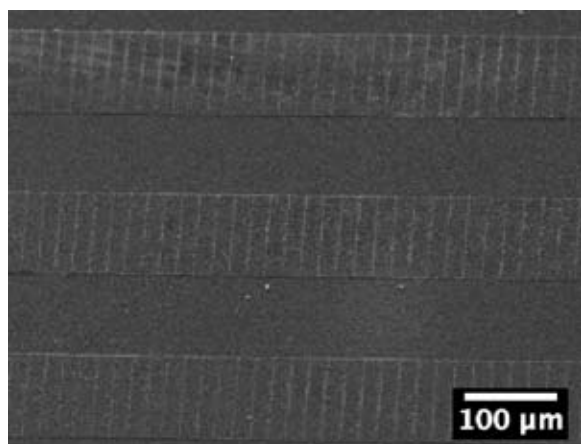


Figure 3: Sample after wire growth.

# The Role of Surfactants in Aqueous Solution Diffusion in Hydrophobic Nanoporous Thin-Film Glasses

Katherine Mackie

Physical Chemistry, Whitworth University

NNIN REU Site: Stanford Nanofabrication Facility, Stanford University

NNIN REU Principal Investigator: Prof. Reinhold Dauskardt, Materials Science and Engineering, Stanford University

NNIN REU Mentor: Taek-Soo Kim, Mechanical Engineering, Stanford University

Contact: kmackie09@whitworth.edu, dauskardt@stanford.edu, tskim1@stanford.edu

## Abstract

Nanoporous organosilicate thin-film glasses are superior candidates for use as ultra-low- $\kappa$  interlayer dielectrics in advanced microelectronic devices. However, it has been recently reported that aqueous solutions containing organic species can readily diffuse in the film, despite the hydrophobic nature of the film, and increase the  $\kappa$  value during processing [1,2]. Of particular concern is the chemical mechanical planarization (CMP) process in which these extremely brittle materials are subjected to applied down force and shear load in the presence of chemically active aqueous solutions. This harsh process not only increases the  $\kappa$  value but also mechanically damages the thin-films. In this study, we demonstrate the role of surfactants, which are essential components of the CMP slurry, on the solution diffusion in nanoporous organosilicate thin-films. Surfactants were found to enhance the diffusion significantly depending on hydrophobic/hydrophilic group lengths and the structure of the surfactant molecule. Direct evidence of surfactant penetration was obtained using x-ray photoelectron spectroscopy after ion etching.

We propose a possible diffusion mechanism using the polymer reptation model to explain surfactant penetration in the nanoporous glass network. Finally, the implication of surfactant diffusion on an optimized CMP process in terms of  $\kappa$  value requirements is presented.

## Introduction

Organosilicate ultra-low- $\kappa$  dielectric glasses are incorporated into interconnect structures of advanced microelectronics to prevent parasitic transmittance. While these glasses are very effective insulators, they are also extremely vulnerable to the diffusion of solution that yields the undesirable result of an increased  $\kappa$  constant. Chemical mechanical planarization (CMP) is an essential process in interconnect fabrication as it results in a flat surface on which the next layer of the structure can be deposited. Now we consider the role of surfactants, which are necessary components of the CMP solution, in diffusion.

## Procedure

Two types of surfactants were considered in this study: monomeric ( $C_mE_n$ ) and Gemini (Surfynol<sup>®</sup>) surfactants. Various surfactant molecular weights and hydrophobic/ hydrophilic group lengths of both types were considered. Initially, solutions made with each surfactant were used, but pure surfactants in liquid phase were also considered. All surfactant solutions were 0.1 weight percent surfactant concentration in deionized water.

The ultra-low- $\kappa$  dielectric thin-film considered in our study was methylsilsesquioxane (MSSQ), which is a hydrophobic, structurally modified form of silicon oxide that has the approximate atomic composition of  $SiO_{1.5}CH_3$  [3]. A porous MSSQ was used that had an average pore diameter of 2.2 nm and a  $\kappa$  constant of 2.3.

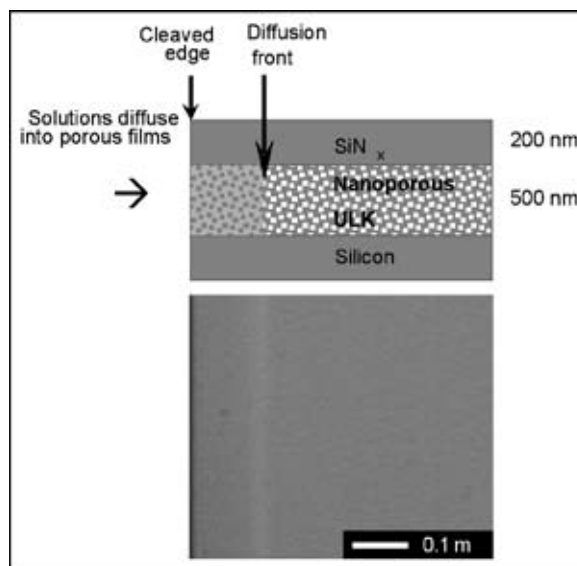


Figure 1: Solution diffusion in MSSQ.

For our study, 500 nm of MSSQ was deposited on a silicon substrate and was capped with an optically transparent silicon nitride layer (200 nm) using the plasma-enhanced chemical vapor deposition system (PECVD). The wafer was then cleaved into  $1.5 \times 1.5$  cm specimens that were placed in Pyrex<sup>®</sup> petri dishes and submerged in either solution or liquid phase surfactant. The diffusion front was then observed and measurements were taken using an optical microscope at 50x magnification (Figure 1).

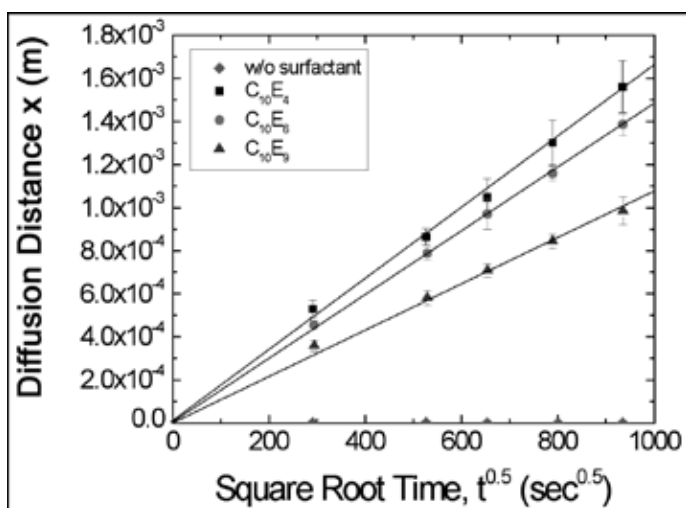


Figure 2: Fick's Law dependent diffusion of linear surfactant solutions.

These techniques were modified from previous studies used to observe the diffusion of aqueous solution [2].

## Results and Conclusions

The diffusion distances of both surfactant solutions and pure surfactants showed a square-root time dependence that is characteristic of Fick's first law:  $x = \sqrt{Dt}$ , where  $x$  is the diffusion distance,  $D$  is the diffusion coefficient, and  $t$  is time (Figure 2). The diffusion coefficient  $D$  was observed to be a function of molecular weight, the hydrophobic/ hydrophilic group lengths, and the molecular geometry of the surfactant. For both the monomeric and Gemini pure surfactants as well as the solutions, the diffusion coefficient increased as the surfactant molecular weight decreased.

It was also observed that as the size of the hydrophilic group length of the surfactants (in both pure surfactant and solution) the diffusion coefficient decreased. The diffusion coefficients of the same surfactant at different concentrations (pure vs. 0.1 % wt) were remarkably similar. So it was determined that the surfactant is the determining factor in diffusion. However, the diffusion coefficients of the linear monomeric surfactants were significantly greater than the diffusion coefficients of the non-linear Gemini surfactants.

Despite the assumption that surfactant molecules are too large to penetrate the nanoporous network, we observed diffusion of pure surfactants. To verify this observation, we used x-ray photoelectron spectroscopy (XPS) and found that there was a significant increase in carbon content (from surfactant molecules) within the diffusion front.

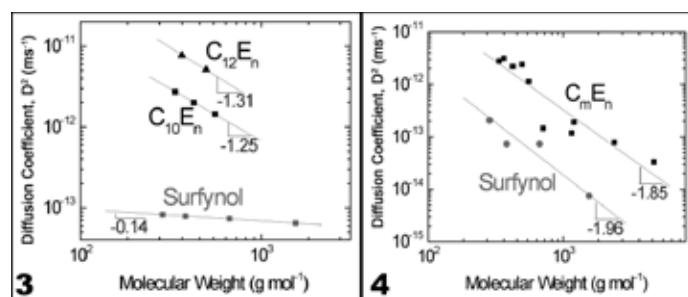


Figure 3: Pure, liquid-phase surfactant  $D$  vs.  $M$ .

Figure 4: Surfactant solution  $D$  vs.  $M$ .

Figures 3 and 4 show each calculated diffusion coefficient  $D$  of all surfactant solutions and pure liquid-phase surfactants plotted against the molecular weight ( $M$ ) of the molecules. It can be noted that the slope of each regression for the surfactant solutions is approximately -2. The polymer reptation model describes the relationship between a polymer's molecular weight and the diffusion coefficient of a polymer melt so that  $D:M^{-2}$ . The polymer reptation model describes the self-diffusion of polymers [4]. Due to the close correlation between this model and the experimental data, we proposed that the surfactant molecules reptate through the nanoscopic pores in MSSQ.

## Acknowledgements

I would like to thank the National Science Foundation for funding. I would also like to thank Professor Reinhold H. Dauskardt and Taek-Soo Kim, Michael Deal and the Stanford Nanofabrication Facility staff, and the National Nanotechnology Infrastructure Network Research Experience for Undergraduates Program.

## References

- [1] S. Kondo, M. Shiohara, K. Maruyama et al., "Effect of the Hydrophilic-Lipophilic Balance (HLB) of Surfactants Included in the Post-CMP Cleaning Chemicals on Porous SiOC Direct CMP," IEEE International Interconnect Technology Conference Proceedings, 172-174 (2007).
- [2] E. P. Guyer, J. Gantz, and R. H. Dauskardt, "Aqueous solution diffusion in hydrophobic nanoporous thin-film glasses," J. Mater. Res. 22 (3), 710-718 (2007).
- [3] M.R. Baklanov, D. Shamiryan, R. Locopi, S.H. Brongersma, K. Maex, Z.S. Yanovitskaya, "Low Dielectric Constant Materials for Microelectronics," J. of Applied Physics 93 (11), 8799 (2003).
- [4] P. G. de Gennes, "Reptation of a Polymer Chain in the Presence of Fixed Obstacles," J. of Chemical Physics 55 (2), 572 (1971).
- [5] G. Strobl, The Physics of Polymers, p. 283, Springer, 1997.

# Charge Transport in Gold Nanocrystal Arrays

David Marsh

Chemistry, University at Buffalo

NNIN REU Site: Nanotech—The UCSB Nanofabrication Facility, University of California, Santa Barbara

NNIN REU Principal Investigator: Dr. Galen Stucky, Department of Chemistry and Biochemistry, Department of Materials, University of California, Santa Barbara

NNIN REU Mentor: Shannon Boettcher, Department of Chemistry and Biochemistry, University of California, Santa Barbara  
Contact: damarsh@buffalo.edu, stucky@chem.ucsb.edu, sboettcher@chem.ucsb.edu

## Abstract

This research focused on gold nanoparticles, and the single electron charging of these nanoparticles as a function of electrochemical potential. We have synthesized a variety of gold nanoparticles, processed them into thin films, and tested these films with cyclic voltammetry (CV) and dual electrode voltammetry (DEV). We have also begun to look at the effect of temperature on the conductivity. We found that conductivity is related to the electrochemical potential applied to the film as well as temperature.

## Introduction

Metal nanoparticles have scientific importance because their electronic properties depend on size, shape and composition. Due to this, these properties can be controlled and manipulated [1]. It is important to understand this phenomenon in order to fabricate devices that utilize these properties. Gold nanoparticles have been studied previously, and the synthesis of purportedly monodisperse particles has been reported [2]. We optimized our synthesis such that the average diameter of our nanoparticles was  $2.0 \pm 0.6$  nm. The size of the nanoparticles is what governs the charging, and this size distribution was narrow enough to give reproducible electrochemical data.

## Experimental Procedure

Gold nanoparticles were synthesized using a modified Brust method [3], with hexanethiol as the stabilizing alkanethiol ligand. After the reduction reaction was complete, ethanol was added and the ethanol-soluble particles were isolated. Concentrated solutions ( $\sim 250$  mg/ml) were prepared in heptane, and thin films were spin-coated (2000 rpm) onto platinum electrodes. For DEV, gold was evaporated on top of the nanoparticle film so that conductivity could be measured through the film. All films were cross-linked in 1,9-nonanedithiol before running CV and DEV.

CV was run under argon, with tetrabutylammonium hexafluorophosphate as the electrolyte in acetonitrile. The reference electrode was Ag/Ag<sup>+</sup>, and the counter electrode was platinum wire. DEV was conducted under the same conditions as CV. Temperature dependence studies were carried out in a cryostat to allow measurements under vacuum and down to liquid nitrogen temperature (77 K).

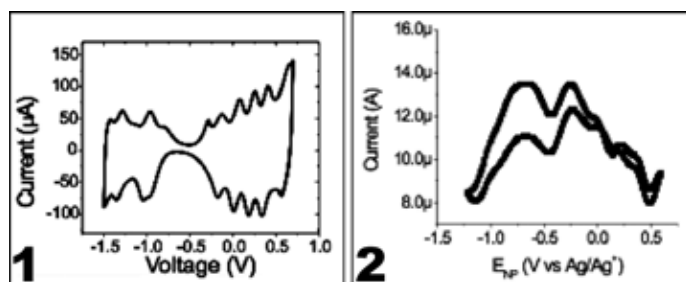


Figure 1: Cyclic voltammetry data.

Figure 2: Dual electrode voltammetry data.

## Results and Discussion

Gold nanoparticles exhibit discrete charging energies and this can be seen on the CV graph (Figure 1). Each peak relates to a single electron charging of half of the nanoparticles, on average. This is an average because the particles aren't all exactly the same size. At the valleys in between the peaks, all the nanoparticles are filled with electrons to the same energy level. At this potential, electron tunneling can only occur if there is thermal activation of an electron to a higher energy level. At the potentials that relate to peaks in the CV graph, electron tunneling can occur without thermal activation since half the nanoparticles already have an electron in a higher energy level. This would mean an increase in conductivity at those specific potentials.

In order to analyze the conductivity as a function of the charge on the nanoparticles, we tested our films with DEV. Figure 2 is the data from the DEV experiment, where conductivity is plotted as a function of potential. From what we know about the CV data, this potential can also be thought of as the charge potential of the nanoparticles ( $E_{NP}$ ). The peaks in the DEV graph occur at similar potentials as the peaks in the CV graph. This supports the claim

$$\sigma = \sigma_0 \exp\left(-\frac{E_A}{RT}\right)$$

$\sigma_0$  = constant  
 $E_A$  = activation energy  
 $R$  = gas constant  
 $T$  = temperature

Figure 3: Arrhenius equation describes thermal activation at low biases.

that these potentials relate to charging of half the nanoparticles, because this data shows that there is an increase in conductivity at these potentials.

### Temperature Dependence

To more fully understand the mechanism of electron tunneling, it is helpful to analyze the effect of temperature. It is also a way of validating the claim that there isn't a need for thermal activation at certain potentials applied to the film. Initially we tested the effect of temperature on conductivity of the uncharged nanoparticle film, to verify that it follows the Arrhenius equation (Figure 3). The Arrhenius equation describes thermal activation of electrons and holds true at low biases. Figure 4 is the temperature dependence data and can be used to calculate the activation energy of an electron. This information would be useful if gold nanoparticles were used in electronic devices.

### Conclusion

Cyclic voltammetry is a good method for analyzing the charge on the nanoparticles. In this experiment, we could detect the addition of a single electron to the nanoparticles by observing a peak. This data matched up with conductivity measurements, since there were peaks in conductivity at nearly the same potentials as the peaks in the CV graph. This is what we would expect because of the lower barrier for electron tunneling when half the nanoparticles are charged. Temperature is related to conductivity by the Arrhenius equation, and we observe this when we measure conductivity at various temperatures.

### Future Work

The next step will be to combine the DEV study with the temperature dependence study. This means driving to the potentials that relate to peaks in the DEV and then running the temperature dependence experiments. This would be a way to confirm the hypothesis that there is little to no thermal barrier for electron tunneling at these potentials. Another experiment would be to vary the electrolyte used for CV and DEV, to see the effect of ion size on the charging of the particles.

### Acknowledgements

I'd like to thank Shannon Boettcher for being a great mentor, as well as the entire Stucky group. Many thanks to the National Nanotechnology Infrastructure Network Research Experience for Undergraduates Program and National Science Foundation for funding.

### References

- [1] Boettcher, S.; Strandwitz, N.; et al. *Nature Materials*, 6, 592-596, (2007).
- [2] Schaaff, T.; Shafigullin, M.; et al. *J. Phys. Chem. B*, 105, 8785-8796 (2001).
- [3] Brust, M.; Walker, M.; et al. *J. Chem. Soc., Chem. Commun.* 801-802 (1994).

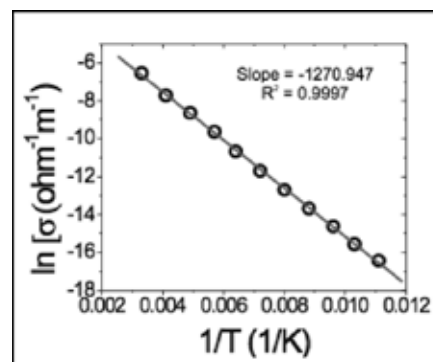


Figure 4: Temperature dependence data; from Arrhenius equation, slope =  $E_A/R$ ,  $E_A = 0.110$  eV.

# Materials Ink Jet Printing of Electronic Structures



**Fabiola Nelson**

**Chemical Engineering, New Jersey Institute of Technology**

*NNIN REU Site: Cornell NanoScale Science & Technology Facility (CNF), Cornell University*

*NNIN REU Principal Investigators: Prof. George G. Malliaras, Dr. Lynn Rathbun, CNF, Cornell University*

*NNIN REU Mentors: Dr. Maria Nikolou, Department of Materials Science and Engineering; Dr. Mandy Esch, Cornell NanoScale Science & Technology Facility; Cornell University*

*Contact: mfn6@njit.edu, ggm1@cornell.edu, rathbun@cnf.cornell.edu, mn262@cornell.edu, esch@cnf.cornell.edu*

## Abstract

We used poly(3,4-ethylenedioxythiophene) doped with poly(styrene sulfonate) (PEDOT:PSS), a commercially available conductive polymer, to fabricate electrodes for disposable sensors. We successfully printed the electrodes using an ink jet printer that utilizes piezoelectric nozzles to dispense the polymer. Printing on silicon wafer and photographic paper yielded good quality electrodes. Our goal was to fabricate electrodes that exhibit low resistance on flexible, inexpensive substrates. The first tasks were to optimize the dimension of the electrode pattern, and then optimize the drop spacing used during the printing process in order to obtain continuous films.

We found that the optimum drop spacing is different for different substrates. The optimum drop spacing for printing on paper is 5  $\mu\text{m}$ . At this drop spacing, the resistance of the electrode measured with a voltmeter is around 80 k $\Omega$ . To achieve an even lower resistance for electrodes that will be used in devices, the following method was used: one layer of PEDOT:PSS was printed, and then a second layer was printed on top of the first one. The resistance of the two layered electrode was around 30 k $\Omega$ .

## Introduction

Currently, commercially available sensors are unable to detect small saliva glucose concentrations. When the use of saliva is coupled with inexpensive, disposable polymer-based sensors, it is possible to create a low cost and painless glucose monitor that can lead to a much more widely used sensor [1]. Inkjet printing is a new technology that is used to print conductive polymers. A simple glucose biosensor with micromolar sensitivity utilizes a conducting polymer transistor with a channel made out of PEDOT:PSS and a platinum (Pt) gate electrode [1]. The ink jet printer allows us to print on inexpensive substrates using PEDOT:PSS as the conductive polymer.

The advantages of using the inkjet-print technology for electrodes used in chemical and biological sensors are the high speed and low cost fabrication as well as the possibility of printing onto flexible substrates [2]. Inkjet printing is one of the most promising technologies for several reasons; one of them is the capacity of depositing micro droplets of 2-12 pl on any surface such as plastics, metals, rubber, glass, silicon wafer [3].

## Experimental Procedure

Initially, we designed the electrode patterns and then using the ink jet printer, we were able to optimize the parameters of the system



Figure 1: Optical microscope image, PEDOT:PSS on paper at 50  $\mu\text{m}$  drop spacing.

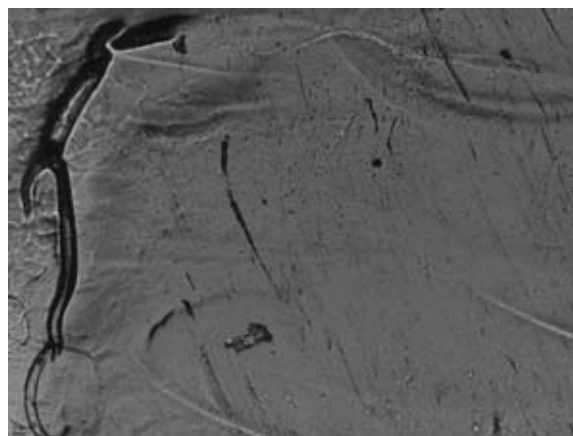


Figure 2: Optical microscope image, PEDOT:PSS on paper at 5  $\mu\text{m}$  drop spacing double layers.

to print PEDOT:PSS electrodes on different substrates (glass slide, Si wafer, and photographic paper). The ideal substrate is inexpensive, flexible, and easy to print on. We predicted that the drops might behave differently on different substrates. In order to obtain continuous films, we changed the drop spacing used during the printing process. The parameter was important because the resistance was affected by drop spacing of the nozzles; large drop spacing could result in a discontinuous film.

Using the molecular vapor deposition (MVD 100) system, we treated the surfaces of the silicon wafer and the glass slide with two chemicals (APTMS and PEG). We investigated whether surface modifications would improve the characteristics of the printed electrodes or not. Photographic paper was used as a substrate to print at different drop spacing, starting with 50  $\mu\text{m}$  to 5  $\mu\text{m}$  single layer printed PEDOT:PSS followed by a double layer printed at 5  $\mu\text{m}$ . We characterized the electrodes printed on photographic paper at 5  $\mu\text{m}$  drop spacing both the single and the double layer by measuring the resistance to see whether we get good quality films. At last we measured the current in order to compare the two final results to see which one performs better.

## Results and Conclusions

As a result of performing these experiments, we came to the conclusion that paper is in fact a suitable substrate to print PEDOT:PSS electrodes. Our experiments showed that printing a double layer of PEDOT:PSS on paper exhibits lower resistance and higher current than all the other substrates under investigation. This result proves that inkjet printed PEDOT:PSS electrodes on paper can be of high quality, thus they can be used in devices.

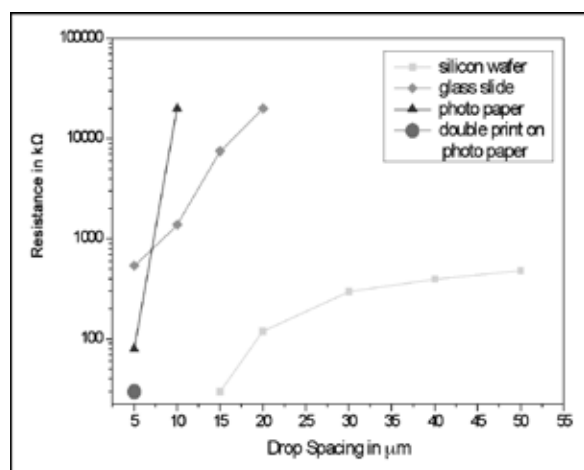


Figure 3: Resistance vs. drop spacing graph with different substrates.

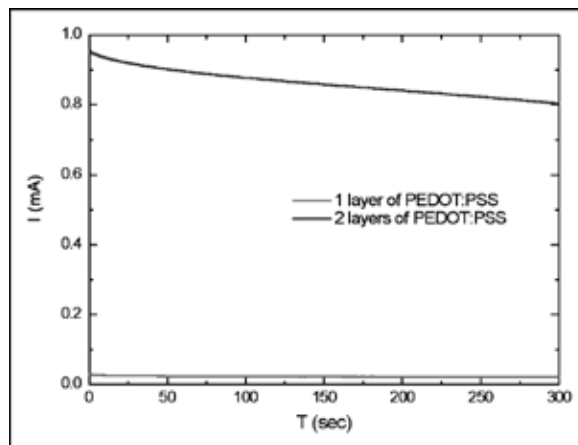


Figure 4: Current vs. time with a drop spacing of 5  $\mu\text{m}$ .

## Future Work

Future work includes the use of the PEDOT:PSS electrodes in electrochemical transistors for chemical and biological applications and the study of their behavior and suitability as part of a circuit.

## Acknowledgments

I would like to thank my principal investigators Prof. George G. Malliaras and Dr. Lynn Rathbun, and my mentors Dr. Maria Nikolou and Dr. Mandy Esch for their support with this project. I would also like to thank the National Science Foundation and the National Nanotechnology Infrastructure Network along with the CNF staff, Intel Foundation, and Cornell University for giving me the opportunity to perform this research.

## References

- [1] Macaya, D. J., Nikolou, M., Takamatsu, S., Mabeck, J. T., Owens, R. M., Malliaras, G. G. "Simple glucose sensors with micromolar sensitivity based on organic electrochemical transistors." *Sensors and Actuators B* 123(2007) 374-378 (2006).
- [2] Mabrook, M. F., Pearson, C., & Petty, M. C. "Inkjet-Printed Polymer Films for the Detection of Organic Vapors." *IEEE Sensors Journal*, Vol. 6, No. 6 (2006).
- [3] Ballarin, B., Fraleoni-Morgera, A., Frascaro, D., Marazzita, S., Piana, C., Setti, L. "Thermal inkjet microdeposition of PEDOT:PSS on ITO-coated glass and characterization of the obtained film." *Synthetic Metals* 146 (2004) 201-205 (2004).

# Fabrication of Low Temperature Solid Oxide Fuel Cells with Ultra-Thin Film Yttria-Stabilized Zircona Electrolytes

Amrita Saigal

Mechanical Engineering, Massachusetts Institute of Technology

NNIN REU Site: Center for Nanoscale Systems, Harvard University

NNIN REU Principal Investigator: Prof. Shriram Ramanathan, School of Engineering and Applied Sciences, Harvard University

NNIN REU Mentor: Dr. Alex Johnson, School of Engineering and Applied Sciences, Harvard University

Contact: saigal@mit.edu, shriram@seas.harvard.edu, acjohns@fas.harvard.edu

## Abstract

Solid oxide fuel cells (SOFCs) have the potential to become the next major breakthrough as an alternative energy conversion device. They use the simple reaction of combining hydrogen and oxygen to produce electricity and water as a by-product. A SOFC is composed of an electrolyte sandwiched between two electrodes (anode and cathode) [1]. In SOFCs, oxygen ions ( $O^{2-}$ ) are transported from the cathode of the fuel cell to the anode through the electrolyte made of a material known as yttria-stabilized zircona (YSZ). Electrons are transported through an external circuit, and the flow of electrons produces electricity. The various electrochemical reaction occurring are—at the anode:  $\frac{1}{2}O_2 + 2e^- = O$ , at the cathode:  $H_2 + \frac{1}{2}O_2 = H_2O + 2e^-$  and overall cell reaction:  $\frac{1}{2}O_2 + H_2 = H_2O$ . The electrochemistry of a SOFC is depicted in Figure 1.

## Introduction

SOFCs operate at very high temperatures of approximately  $800^\circ\text{C}$ - $1000^\circ\text{C}$  and this leads to two major problems. First, SOFCs have to be heated up slowly or else they will break due to differential thermal expansion. Secondly, most metals oxidize or corrode at the high operating temperature of SOFCs and therefore stop conducting oxygen ions across the electrolyte. The operating temperature of the fuel cell cannot simply be reduced because the ionic conductivity of the YSZ electrolyte is reduced at lower operating temperatures [2]. Ionic resistance,  $R = \rho t/A$  where resistivity  $\rho \sim e^{Ea/kT}$  ( $Ea \sim 0.9$  eV). Therefore, decreasing the thickness,  $t$ , of the electrolyte will allow for lower operating temperatures,  $T$ . The optimal SOFC operating temperature is  $\sim 300^\circ\text{C}$ , since this is the temperature at which the anode and cathode can perform catalytic activity, and metal can also be used for other components of the fuel cell since they will no longer melt. In order to have a SOFC operate at  $300^\circ\text{C}$ , the thickness of the YSZ electrolyte should be around 50 nm.

The second goal of the research was to study the porosity of platinum, which was used for making the anode and cathode, under different sputtering conditions so as to create electrodes with smaller pores to allow for more surface area for the oxygen ions, hydrogen and electrons to travel through and react on.

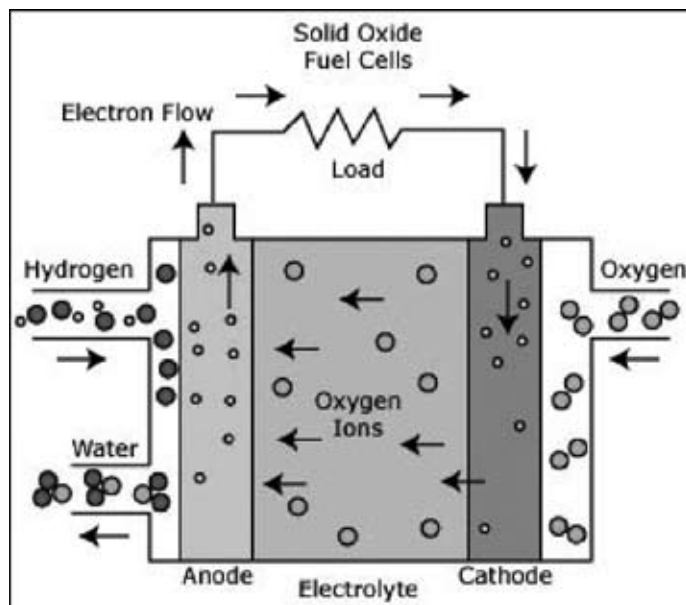


Figure 1: Electrochemistry of a solid oxide fuel cell.

## Materials and Methods

Fabrication of a SOFC begins with a silicon wafer  $\sim 500$   $\mu\text{m}$  coated with silicon nitride ( $Si_3N_4 \sim 200$  nm) on both sides using the process of low pressure chemical vapor deposition. Silicon nitride serves as an insulator to prevent any unwanted reactions from occurring between the YSZ and Si, since both are very good conducting materials. The next step is to sputter a thin layer of YSZ, the electrolyte, on top of the  $Si_3N_4$  at a pressure of 5 mTorr, 100W power for 30 min to produce a thickness of  $\sim 40$  nm. The next step is to pattern the back side of the chip and remove the patterned area of  $Si_3N_4$  using reactive ion etch. The top of the chip is then patterned and a thin layer of titanium (Ti) is sputtered on the top of the chip at 4 mTorr, 250W for 2 min to produce a thickness of  $\sim 5$  nm. Ti serves as an adhesive between the platinum electrodes and YSZ electrolyte. Platinum (Pt) is then sputtered on top of the Ti at 4 mTorr, 250W for 5 min to produce dense platinum with thickness of  $\sim 100$  nm.

The reason for using dense platinum is that it has better electrical properties than porous platinum, so anywhere the platinum is not in direct contact with the YSZ electrolyte, as is found with the platinum on top of the titanium, there should be dense platinum.

The next step is to perform lift-off to remove the excess Ti/Pt coating. Pt is then sputtered throughout the top of the chip at 75 mTorr, 250W for 15 min to produce porous platinum which serves as the top electrode. Finally, in order to study the porosity of platinum under different conditions, we sputtered Pt by varying the following parameters; time from 5-80 min, pressure from 4-100 mTorr, and power from 100-250W, to produce platinum films with different thicknesses.

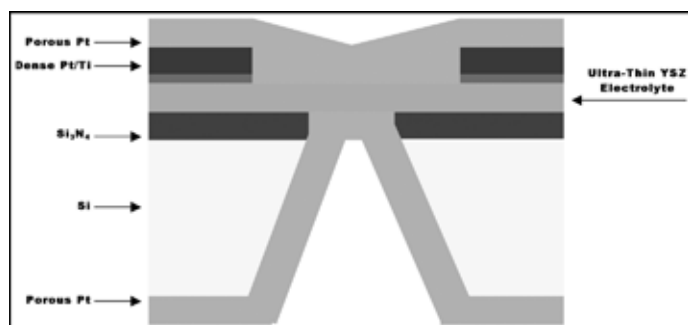


Figure 2: Fabricated solid oxide fuel cell.

## Results and Discussion

Figure 2 shows the final fabricated solid oxide fuel cell. It can be seen from Figure 3 that increasing the thickness of the platinum yields larger pores with a relatively linear relationship, although neither pressure nor power have a significant effect on pore size. A possible explanation for this increase in pore size is that as more Pt atoms are added, they build outward from the existing grains, mainly upward, but also sideways so that some of the existing grains merge together to form larger pores.

## Conclusions and Future Work

A SOFC with an ultra-thin YSZ electrolyte was successfully fabricated. There is a strong correlation between thickness of sputtered platinum coating and pore size where the pore size linearly increases with coating thickness. Future work includes

measuring the conductivity of these fabricated SOFCs to verify that the conductivity does not decrease significantly at lower operating temperatures. Also, based on successful sputtering of platinum coatings for the anode and cathode, the next step is to create a lanthanum strontium cobalt iron oxide (LSCF) cathode and a nickel YSZ oxide anode, which are known to work well as electrodes to replace the expensive platinum.

## Acknowledgments

I would like to thank Prof. Shriram Ramanathan, Drs. Alex Johnson and Kathryn Hollar for their help and support as well as Harvard's Center for Nanoscale Science, National Nanotechnology Infrastructure Network Research Experience for Undergraduates Program and National Science Foundation for funding.

## References

- [1] Hallie, S. Fuel cell materials and components. *Acta Materialia* 51: 5981-6000. 2003.
- [2] Fasching, R., H. Huang, M. Nakamura, F. Prinz, Y. Satio, and P. Su. High-Performance Ultrathin Solid Oxide Fuel Cells for Low-Temperature Operation. *Journal of the Electrochemical Society* 154: B20-B24. 2006.

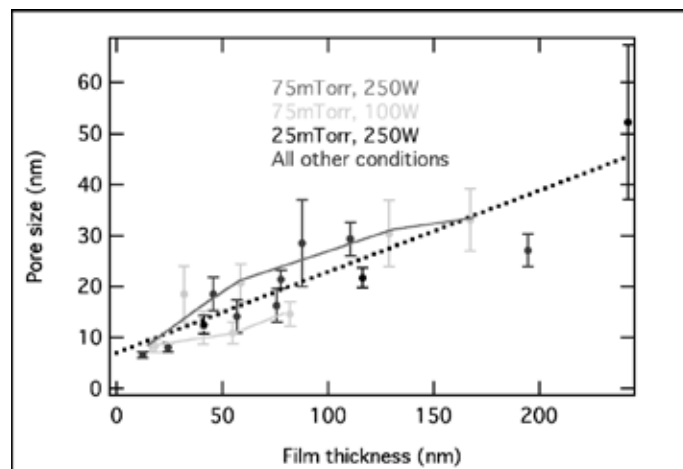


Figure 3: Effect of platinum thickness on pore size.

# Probing Nanostructures of Biorenewable Polyurethane Collapsed Foams

**Ryan J. Seelbach**

Physics, Beloit College

*NNIN REU Site: Minnesota Nanotechnology Cluster, University of Minnesota-Twin Cities*

*NNIN REU Principal Investigator: Dr. Christopher W. Macosko, Chemical Engineering and Materials Science, University of Minnesota-Twin Cities*

*NNIN REU Mentor: Ling Zhang, Chemical Engineering and Materials Science, University of Minnesota*

*Contact: rseelbach@gmail.com, macosko@umn.edu, zhang@cems.umn.edu*

## Abstract

Petroleum-based materials comprise the dominant resource going into the manufacturing of flexible foams. The rising cost of petroleum is providing the opportunity to implement vegetable-based resources into this expanding industry. 100% vegetable-based polyurethane (PU) flexible foams have been developed to exhibit viscoelastic properties comparable to their petroleum ether analogues.

Four vegetable-based collapsed foam samples were prepared and their glass transitions, mechanical moduli, and phase morphologies were studied. Glass transition temperatures and moduli were analyzed via differential scanning calorimetry (DSC) and dynamic mechanical analysis (DMA). Polyurea hard domain spacings were measured and visualized using small/wide angle x-ray scattering (SWAXS) and tapping mode atomic force microscopy (AFM). It was found that the soft domain glass transition temperature decreases as the molecular weight of the polyol structure increases.

## Introduction

The chemical structure inherent to the vegetable oils varies in the degree and location of unsaturation, and determines the overall length of the fatty acid chains. By extending the polyol chain at the unsaturation points, the overall chain length increases. The goal of this experiment is to examine the effects of fatty acid chain length (i.e. polyol molecular weight) to thermal properties and phase morphology of PU foam.

During foaming, two competing reactions give rise to the phase separation of hard and soft domains. The gelling reaction is the polymerization of polyol with isocyanate to form the polyurethane soft segment (SS). The blowing reaction is the polymerization of isocyanate and water to form polyurea hard segments (HS). The hard segments eventually agglomerate during the reaction to form phase-separated hard domains throughout the continuous soft phase.

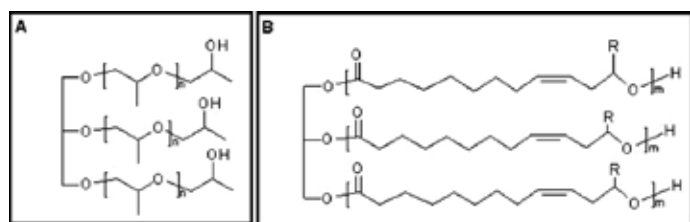


Figure 1: A] Petroleum polyether polyol. B] Vegetable-based polyol.

## Experimental

### Materials

The vegetable-based polyols used for this experiment were 1K, 2K, 3K, and 4K molecular weight polycondensate triols, Figure 1. These materials were polymerized using trimethylol propane (TMP) starter and ricinoleic acid via esterification synthesis. Arcol F3022 (Bayer Corporation), a petroleum polyether polyol that is comparable to the 3K polyol, Figure 1, was also used. An 80/20 mixture of 2,4 and 2,6-toluene diisocyanate (TDI) was stoichiometrically balanced to completely react with the water and polyols. The blowing catalyst used to accelerate the blowing reaction was DABCO®BL-11 (Air Products).

### Procedure

All samples were made into collapsed foams (CF). Polyol, water, and catalyst were added to a 50 mL plastic beaker. TDI was added last and hand mixed for 10-20 minutes in a silicon oil heat bath at 55°C until the blowing reaction was complete, and the mixture was highly viscous or crumbling. The foam was poured into a 1.5 mm thick steel mold with 25 mm diameter circular cutouts. The mold was sandwiched between a layer of Teflon® followed by a steel plate. The plates were placed in a hydraulic press (Carver, Auto Series, model 3895) at 100°C and 15000 lbs. force for 1.5 h.

## Characterization

**Differential Scanning Calorimetry:** DSC (Q1000, TA Instruments) was used to observe the SS glass transition temperatures. About 6-10 mg of the CF was placed and sealed into an Al hermetic pan. Heat flow data was taken over a temperature range from  $-100^{\circ}\text{C}$  to  $200^{\circ}\text{C}$  at a rate of  $10^{\circ}\text{C}/\text{min}$ .

**Dynamic Mechanical Analysis:** DMA (ARES II, TA Instruments) measured the elastic modulus,  $G'$ , and loss modulus,  $G''$ , over the temperature range of  $-100^{\circ}\text{C}$  to  $200^{\circ}\text{C}$ . CF samples were cut to 12.65 mm width and placed in a rectangular torsion apparatus. A strain of 0.05% was applied and data was taken at a frequency of 3 rad/s.

**Small/ Wide Angle X-Ray Scattering:** SAXSess instrument (Anton Paar), operated at 12 kW and 50 mA, was used to determine hard domain spacings in samples. CF samples were cut and placed in a Cu sample holder and exposed to the x-ray source for 10 min. Scattering profiles were normalized to sample thickness.

**Atomic Force Microscopy:** An atomic force microscope (AFM) (Nanoscope III Multimode, Digital Instrument) was mounted on an optical microscope (Nikon). Tapping mode images were taken using a Si cantilever with a tip radius of about  $100\text{\AA}$  and an oscillating resonant frequency of  $\sim 240\text{ kHz}$ . All images were taken under ambient conditions. Tapping oscillations were conducted in the repulsive regime and with resolution of  $512 \times 512$  pixels.

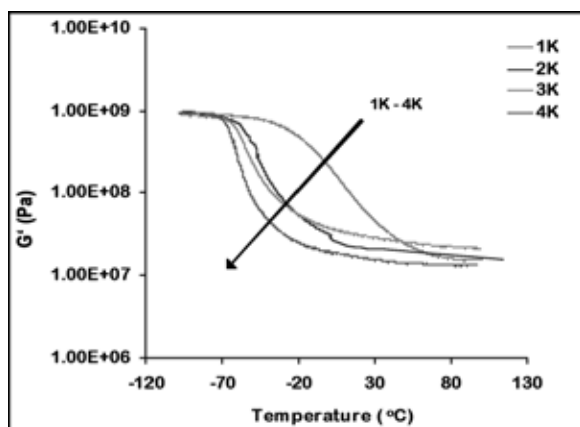


Figure 2: Dynamic mechanical analysis.

## Results and Discussion

With increasing the weight of the vegetable oil structure, the PU foam's  $T_g$  decrease as seen in Figure 2. The initial drop in  $G'$  data around  $-60^{\circ}\text{C}$  corresponds to the increase in SS mobility. The temperature is the  $T_g$  of the soft domains. SAXS, Figure 3, gives an average value of hard domain spacings; a characteristic shared with the petroleum analogues. AFM provides a localized map of the phase morphology. A 500 nm phase image of 4K MW polyol is shown in Figure 4. Hard domains are brighter regions, and

soft domains are darker regions. The phase scale was adjusted to show a clear contrast between the two regions. The hard domains agglomerated into tiny sphere-like orbs and distributed in the SS matrix. All images were plane-fitted to remove large scale surface curvature for better height profile displays. From experimental results, biorenewable polyols can potentially replace petroleum feedstock, making a novel substitute in industrial production of PU flexible foams. Thermal properties, such as  $T_g$ , of vegetable based PU can be tuned via the control of polyol MW.

## Acknowledgements

The author would like to thank the Chemical Engineering and Materials Science Department at the University of Minnesota for allowing him to gain exposure into graduate study. The knowledge will be invaluable to his future. Also, thanks to the National Nanotechnology Infrastructure Network Research Experience for Undergraduates Program funding for this wonderful internship.

## References

- [1] Zhang et al. Comparison of Polyurethane Flexible Foams: Polyether vs. Soybean Oil-based Polyols. Submitted for Pub.

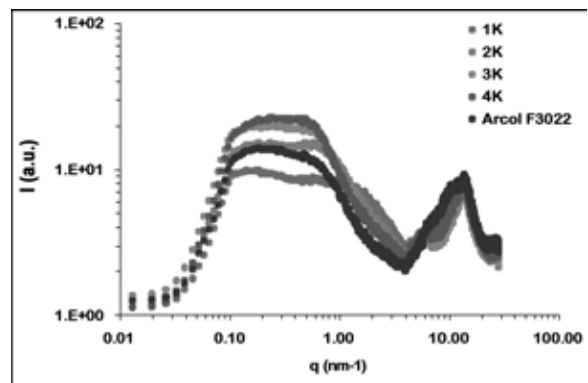
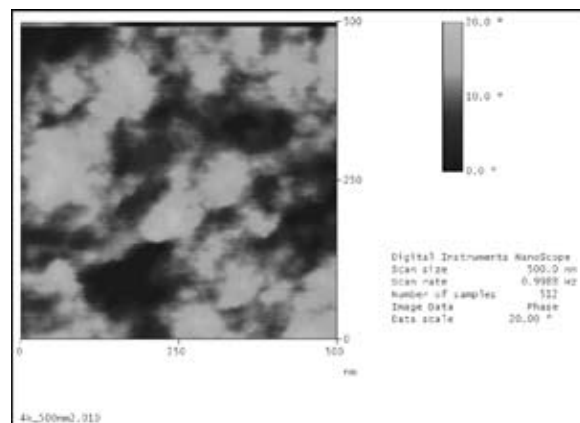


Figure 3: Small/wide angle x-ray scattering.

Figure 4: Atomic force microscopy image.



# Nanostructured Photovoltaics Using Porous Alumina Templates as Structure-Directing Agents

Jessica Sherman

Department of Chemistry, University of Kentucky

*NNIN REU Site: Nanotech—The UCSB Nanofabrication Facility, University of California, Santa Barbara*

*NNIN REU Principal Investigators: Profs. Martin Moskovits and Galen Stucky, Department of Chemistry, University of California, Santa Barbara*

*NNIN REU Mentor: Martin Schierhorn, Department of Chemistry, University of California, Santa Barbara*

*Contact: jes.carbon@gmail.com; mmoskovits@lts.ucsb.edu, stucky@chem.ucsb.edu; mschierhorn@chem.ucsb.edu*

## Abstract

Nanostructured architectures for use in type II heterojunction photovoltaic devices are explored in this report. Porous aluminum oxide (PAO) templates were employed as structure-directing agents in the electrochemical synthesis of cadmium selenide (CdSe) nanorod arrays. Arrays fabricated using a cyclic voltammetry (CV) method were subjected to photoelectrochemical measurements to determine the effect of rod dimensions on device performance. Additionally, an alternating current (AC) electrolysis method for CdSe deposition was developed and optimized.

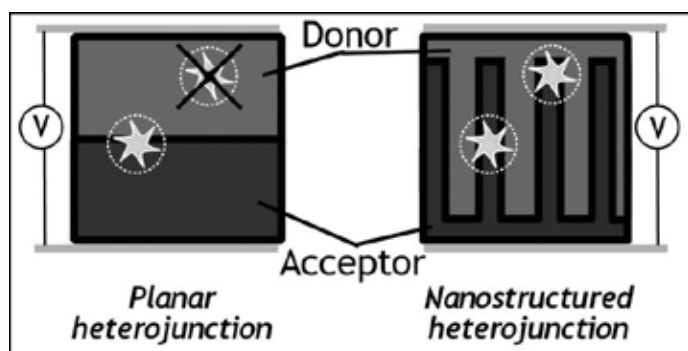


Figure 1: Solar cell schematic. Stars represent photoexcitation; X denotes exciton recombination.

## Introduction

Separation of electrostatically bound charge-carrier pairs in photovoltaics is crucial to proper device function. Following photoexcitation in a solar cell, an exciton (electron-hole pair) can only diffuse a finite distance before recombination occurs. Semiconductor nanorod arrays provide a highly ordered device architecture in which an exciton can reach the donor-acceptor heterojunction prior to recombination. This strategy (Figure 1) could produce highly efficient photovoltaics.

Free-standing semiconductor nanorod arrays can be fabricated using PAO templates [1]. CdSe, due to its high electron mobility and wide (1.77 eV) bandgap, was an attractive material for this study. It has been studied in photoelectrochemical cells, which provide a means to analyze photocurrent generation in nanorod arrays with varying dimensions [2,3]. The liquid electrolyte junction eliminates problems associated with poor interface morphology found in solid bulk heterojunctions. However, since photovoltaic device operation requires a transparent electrode,

usually indium tin oxide (ITO), we also sought a synthetic method that would create nanorod arrays with a surface onto which ITO could be affixed. The known CV method deposits nanorods onto a conductive substrate, but requires acidic solution which etches ITO [4]. This led us to AC electrolysis, which plates material directly onto a thin insulating layer of alumina in the pores of the template and provides a semiconductor film at the base of the rods [5].

## Experimental Procedure

**Photoelectrochemistry:** PAO templates were prepared according to literature methods and were anodized with either sulfuric acid (45 nm pore width) or oxalic acid (60 nm pore width) [1]. Nanorod arrays were fabricated using the PAO templates and a known CV method, and characterized using x-ray photoelectron spectroscopy (XPS) [4]. The arrays were annealed for 30 minutes at 400°C under argon to increase crystal grain size. The gold backing was then attached to copper wire and the assembly was coated in epoxy, leaving the wire tip and CdSe nanorods exposed. Etching in 5 M NaOH for 3 hours removed the alumina template. The photoelectrochemical cell used a 0.2 M solution of NaOH, Na<sub>2</sub>S and S as the electrolyte and a Pt mesh counterelectrode. All measurements were taken under argon.

**AC Electrolysis:** PAO templates were anodized in oxalic acid; some were also subjected to a 15 minute pore-widening soak in H<sub>3</sub>PO<sub>4</sub>. A solution of 0.01M CdCl<sub>2</sub> in DMSO was heated to 180°C under argon. Se was then added to saturation. The PAO template and a graphite rod were submerged in this solution and used as electrodes as an AC potential was applied. CdSe nanorod growth on the template was then characterized by scanning electron microscopy (SEM) and energy-dispersive x-ray spectroscopy (EDX).

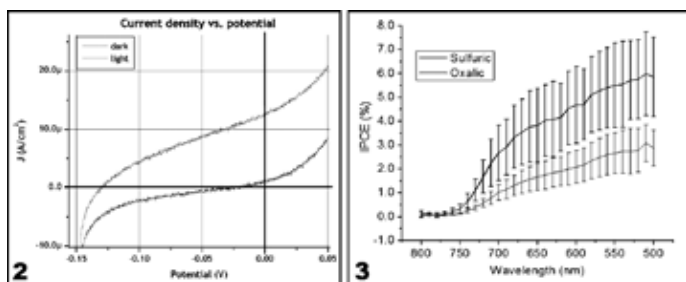


Figure 2, left: Representative  $J$ - $V$  curve for photoelectrochemical cells.

Figure 3, right: Efficiency of nanorods produced using sulfuric vs. oxalic acid anodization.

## Results

XPS measurements for the nanorods produced using the CV method revealed an average 45:55 Cd:Se stoichiometry. (Any deviation from 1:1 stoichiometry indicates point defects within the lattice, which may act as charge-carrier traps.) The nanorod arrays displayed some photoresponse in photoelectrochemical device assemblies (Figure 2), but the low short-circuit current density ( $12.5 \mu\text{A}/\text{cm}^2$ ) indicated that optimization is necessary. The open-circuit potential (vs. Pt counterelectrode) was measured at 0.13 V. Figure 3 illustrates the efficiency (expressed as incident photons converted to electrons, or IPCE) of the sulfuric and oxalic acid-anodized templates. Sulfuric acid-anodized PAO templates produced more efficient nanorods than did oxalic acid-anodized templates. The absorption onset near 700 nm corresponds to the CdSe bandgap. The electrolyte solution absorbed strongly below 500 nm, precluding any efficiency measurements in that range.

The AC electrolysis method for nanorod array fabrication was explored using PAO templates with 200 nm average pore depth. This length of nanorods, in addition to uniform, 100 to 200 nm CdSe films, is expected to allow effective photovoltaic device fabrication. The nanorods were deposited by applying 30 V AC to a PAO template for 30 minutes. Alternatively, a pore-widened PAO template produced nanorod arrays with the appro-

priate CdSe film thickness with application of 45 V AC for 15 minutes. EDX analysis indicated a Cd:Se stoichiometry of 61:39. Decreasing the concentration of the  $\text{CdCl}_2$  solution may bring the stoichiometry to the desired 1:1 ratio.

## Future Work

The device fabrication process for CdSe arrays in photoelectrochemical cells requires optimization. Additionally, efficiency measurements of flat thin films of CdSe would allow a comparison to be drawn between thin film and nanorod performance.

The arrays produced using AC electrolysis are attached to thin films of CdSe, which may provide a useful surface onto which an ITO electrode may be sputtered. Once ITO is applied, the PAO template can be etched away, and a donor material and back electrode can be added to the photovoltaic assembly. Fabrication of proof-of-concept devices is underway.

## Acknowledgments

Thanks to Martin Moskovits, Galen Stucky, Martin Schierhorn, Angela Berenstein, NSF, UCSB, Institute for Collaborative Biotechnologies, and the National Nanotechnology Infrastructure Network Research Experience for Undergraduates Program.

## References

- [1] O'Sullivan, J.P.; Wood, G.C. Proc. R. Soc. London, Ser. A, 1970, 317, 511.
- [2] Miller, B.; Heller, A.; Robbins, M.; Menezes, S.; Chang, K. C.; Thomson, Jr., J. J. Electrochem. Soc., 1977, 124 (7), 1019.
- [3] Ellis, A. B.; Kaiser, S. W.; Wrighton, M. S. J. Am. Chem. Soc., 1976, 98 (22), 6855.
- [4] Norvell, E. NNIN REU Research Accomplishments, 2006, 76.
- [5] Routkevitch, D.; Tager, A. A.; Haruyama, J.; Almawlawi, D.; Moskovits, M.; Xu, J. M. IEEE Trans. Electron Devices, 1996, 43 (10), 1646.

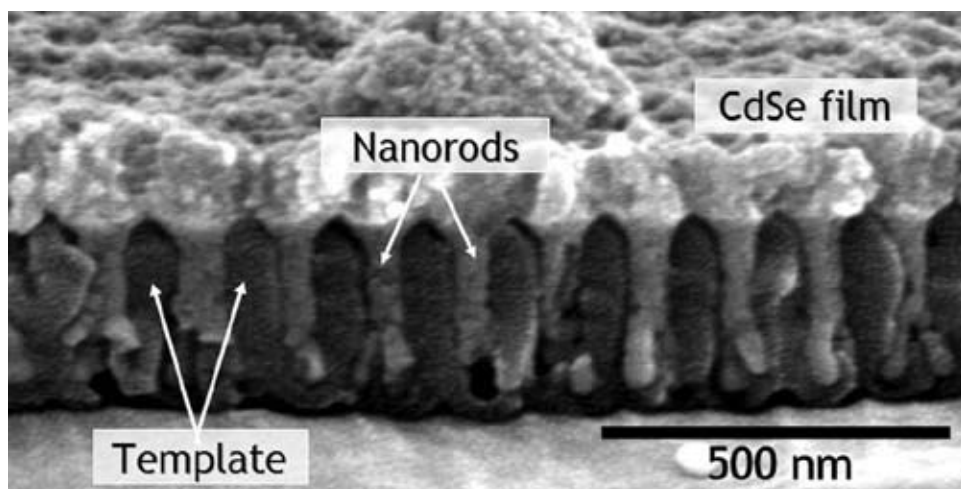


Figure 4: SEM micrograph of nanorod array produced using AC method.

# Functionalization of Silicon Nanoparticles for Hyperpolarized Magnetic Resonance Imaging

**Derek Smith**

Chemical Engineering, University of Rochester

*NNIN REU Site: Center for Nanoscale Systems, Harvard University*

*NNIN REU Principal Investigator: Prof. Charles Marcus, Department of Physics, Harvard University*

*NNIN REU Mentor: Dr. T. Fettah Kosar, Center for Nanoscale Systems, Harvard University*

*Contact: dsmith30@mail.rochester.edu, marcus@harvard.edu, fkosar@cns.fas.harvard.edu*

## Abstract

Magnetic resonance imaging (MRI) is used in the medical field for visualizing organs, tissues and structures within the body. Although MRI is widely used, it suffers from problems in certain cases due to overwhelming background signal. Silicon nanoparticles can be functionalized and introduced into the body as contrast agents, and they possess unique properties to correct many of the shortcomings of MRI. This project focuses on functionalizing silicon nanoparticles with specific molecules to target and image tumors or specific tissues and organs.

## Introduction

MRI is a non-invasive medical imaging technique used to detect physiological defects within living tissues. It utilizes radio-frequency signals to measure the magnetic relaxation times of nuclei found in the body. Depending on the type of tissue, these relaxation times will differ, and through the use of magnetic gradients, a three-dimensional image of the scanned area can be created [1]. However, MRI currently suffers from image contrast issues when attempting to distinguish between healthy and cancerous tissue at small scales, and when dealing with organ systems that are in constant motion [1]. Silicon nanoparticles, which can be hyperpolarized, have the potential to correct these shortcomings.

Normal MR images are limited due to their imaging source. Since they are based on imaging the hydrogen nuclei found in water in the body, noise from other areas of the body will be a constant problem due to the abundance of water. In contrast, silicon is normally present in the body in insignificant amounts. Hence, silicon nuclei in hyperpolarized silicon nanoparticles can be imaged in place of hydrogen nuclei. This approach allows for the potential to target specific areas of the body without interference from background noise.

The aim of this project is to functionalize silicon nanoparticles to make them effective magnetic resonance imaging agents. Although silicon is already biocompatible, the surface of the nanoparticles must be modified to increase retention times in the body and to allow for specific targeting of organ systems or tumors. Functionalization of the nanoparticles is the first step to achieving both of these goals.

## Experimental

The silicon nanoparticles were prepared by grinding down silicon wafers using a ball mill under varying conditions. These particles were then characterized by size using a scanning electron microscope (SEM) or by dynamic light scattering (DLS). Figure

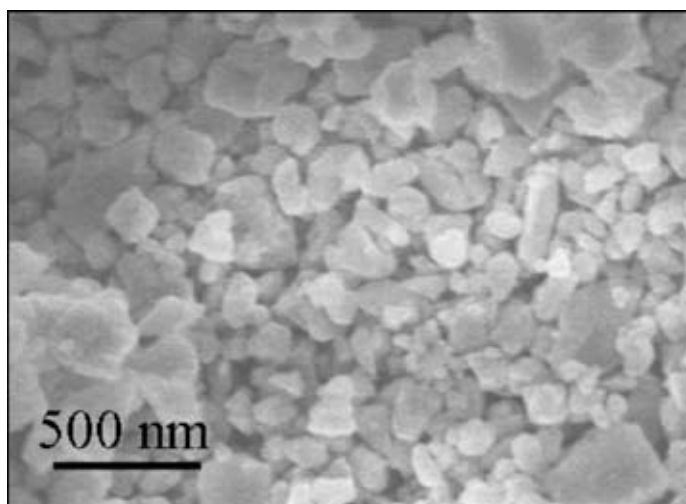


Figure 1: SEM image of silicon nanoparticles.

1 shows the resulting nanoparticles. The particles shown have an average diameter of about 200 nm.

The functionalization of the silicon nanoparticles makes use of organosilane chemistry. The organosilane of choice for this project is 3-aminopropyltriethoxysilane (APTES). As seen in Figure 2, APTES reacts with the oxide layer on silicon through a known mechanism. The amine group present on this organosilane allows for further modification, and also provides a means to determine the success of the reaction by looking for the presence of nitrogen using elemental analysis techniques. Functionalization of a silicon surface using APTES has previously been done on silicon wafers, and attempts have been made to optimize the reaction on such surfaces [2]. Using these reports as a starting point, the organosilane reaction was first tested on small wafer squares to find the optimal reaction

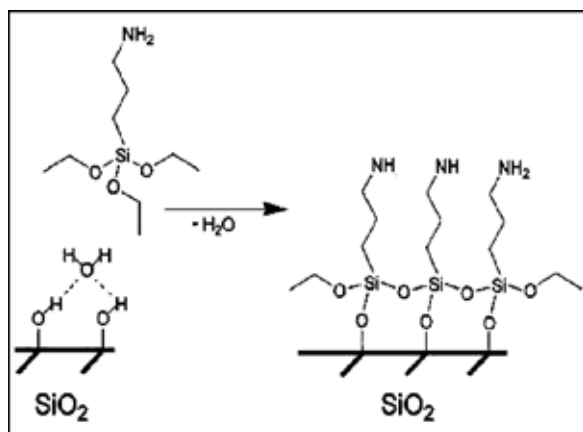


Figure 2: Reaction between APTES and native oxide on silicon [2].

conditions. Untreated, Piranha etched (2:1 (v/v) sulfuric acid to hydrogen peroxide), and hydrofluoric acid (HF) etched wafers were evaluated under varying reaction parameters. The reaction was carried out under dry nitrogen atmosphere in anhydrous toluene. X-ray photoelectron spectroscopy (XPS) was used to determine if APTES was present on the surface of the wafers. We looked for a nitrogen peak that signaled the presence of APTES and compared the relative sizes of this peak.

Once the ideal conditions were determined, the silicon nanoparticles were functionalized using the same protocol. Untreated and etched nanoparticles were used to test for effects of surface treatment on the functionalization reaction, as well as for changes in the MRI properties of the nanoparticles. Both XPS and Fourier transform infrared spectroscopy (FTIR) were used to analyze the surface chemistry of the particles.

## Results and Conclusions

XPS results from the wafers indicated that the optimal reaction conditions for all surface treatments were a 24 hour reaction in 1:9 APTES in toluene. Although both XPS and FTIR were used in the analysis of the nanoparticle reactions, FTIR produced the most consistent results. The primary regions compared in the FTIR graphs were the C-H stretching region from 2800 to 2950  $\text{cm}^{-1}$  and the N-H stretching region from 1500 to 1650  $\text{cm}^{-1}$ , both of which should only be present in those particles that had APTES on the surface. As seen in Figure 3 and 4, all three reacted particle sets exhibited relatively strong C-H peaks, particularly the “No Etch” and “Piranha Etch” particles. The N-H regions show a similar trend. These results are consistent with the presence of APTES on our nanoparticles. Further testing is needed to quantify the extent of functionalization on the silicon nanoparticle surface and confirm these results.

## Future Work

Currently, work is being done to react the amine functional group present on the surface of the reacted silicon nanoparticles with

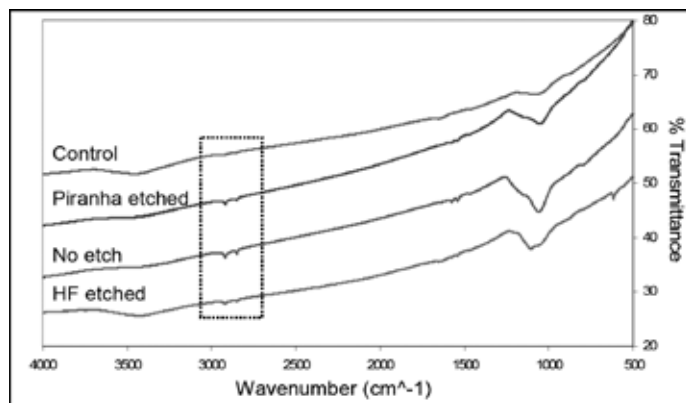


Figure 3: Full FTIR spectrum of reacted nanoparticles.

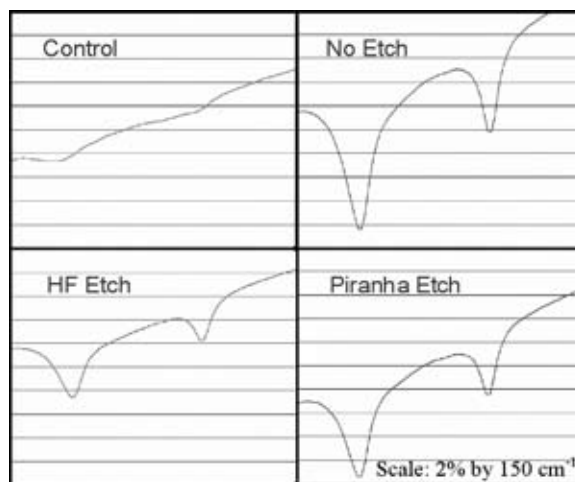


Figure 4: FTIR close-up of dashed area, showing C-H stretching region.

monofunctional poly(ethylene glycol)-succinimidyl  $\alpha$ -methylbutanoate (mPEG-SMB), a functional group which will allow the nanoparticles to have a longer retention times *in vivo*. These functionalized particles will then be imaged *in vivo*.

## Acknowledgements

I would like to thank Prof. Charles Marcus, Dr. T. Fettah Kosar, and Marcus group members Jonathan Marmurek, Rob Barton, and Jacob Aptekar. I'm also indebted to CNS, Harvard SEAS, the National Nanotechnology Infrastructure Network (NNIN) REU Program and the NSF for their support.

## References

- [1] Weishaupt, Dominik; Köchli, Victor D.; Marincek, Borut. “How does MRI work?,” Springer: New York, 2003.
- [2] Howarter, J.A. and Youngblood J.P.; Langmuir, 22, 11142-11147 (2006).

# Spontaneous Alignment in Self-Assembled Block Copolymers for Nanolithography

**Mikael Witte**

Physics and Mathematics, St. Olaf College

*NNIN REU Site: Minnesota Nanotechnology Cluster, University of Minnesota-Twin Cities*

*NNIN REU Principal Investigator: Dr. Marc Hillmyer, Chemistry, University of Minnesota-Twin Cities*

*NNIN REU Mentor: Dr. Chris Leighton, Chemical Engineering and Materials Science, University of Minnesota-Twin Cities*

*Contact: witem@stolaf.edu, hillmyer@chem.umn.edu, leighton@tc.umn.edu*

## Abstract

Block copolymers were used to create self-organizing templates for pattern transfer. The goal of the templates was to exceed  $10^{12}$  features per square inch for use in magnetic media. The cylinder forming diblock copolymer polystyrene-poly lactide (PS-PLA) has been observed to spontaneously align with cylinders of PLA oriented perpendicular to the substrate in a PS matrix after thermal annealing. The project examined spontaneous alignment of PS-PLA thin films of varying thickness on silicon (Si) and nickel-iron / gold (NiFe/Au) substrates without thermal annealing, and compares PS-PLA thin films with previously characterized polystyrene-polyisoprene-poly lactide (PS-PI-PLA) triblock terpolymer thin films. In addition, the project included general observations of the pattern transfer process. One hypothesis was that PS-PI-PLA forms a perpendicular cylindrical pattern because of the energetic preference for PI for the film surface, thus there should be no perpendicular alignment with PS-PLA.

## Introduction

The capacity of magnetic media is approaching an upper limit with current optical lithography techniques. In order to create new media with capacities in the terabit range, novel techniques must be found. Pattern transfer is one such technique, but there remain some obstacles with the block copolymer method, such as attaining long-range order (on the scale of  $\sim 1 \text{ cm}^2$ ), choosing the ideal block copolymer for its feature size and chemical properties, and perfecting the pattern transfer process to reproducibly create the desired pattern on a magnetic film. The ideal block copolymer has an average feature size of approximately 10 nm, with the minority component(s) self-assembling into a hexagonal pattern of cylinders aligned perpendicular to the substrate. Optimizing the pattern transfer process means, first and foremost, ensuring that the pattern is transferred. This is accomplished by trying to make the template an etch resist. Eliminating unnecessary steps in the process is also important, as this can increase reproducibility and minimize costs.

## Experimental Procedure

The synthesis of PS-PLA is described elsewhere [1-3]. The sample (labeled MDR-II-85) we used had an average molecular weight of 60 kg/mol, determined from GPC, with a 2:1 mass ratio of PS to PLA and a polydispersity of 1.05. The substrates were Si/SiO<sub>2</sub> wafers of approximately 1 cm<sup>2</sup>. Six were left as naked Si/SiO<sub>2</sub> and the other six were prepared with 5 nm NiFe (80:20 Ni:Fe) and a 5 nm Au endcap sputtered on at room temperature. Six PS-PLA solutions of varying concentration were created by

adding 2 mL of chlorobenzene to varying masses of PS-PLA, from 15 mg to 35 mg. Then the solution was spin-coated onto the wafers at a constant spinning speed of 2000 rpm.

Film thickness was measured with grazing angle x-ray reflectivity (GIXR). Other characterization was performed with a Nanoscope III atomic force microscope in tapping mode. After initial characterization, the samples underwent a 45-minute 0.5 M NaOH bath followed by a 5-minute rinse in distilled water and argon drying to degrade and remove the PLA component. The samples were characterized again with the atomic force microscope (AFM).

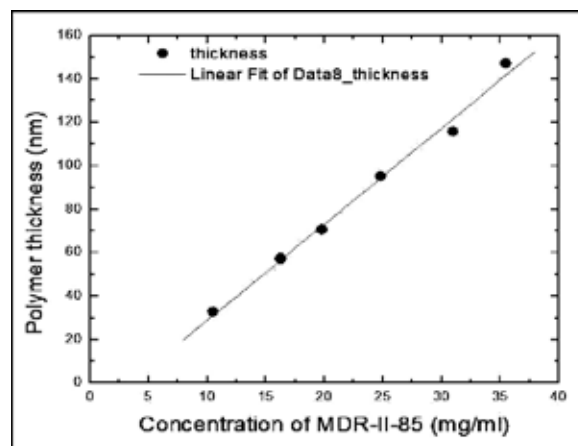


Figure 1: Thin film thickness in nm as a function of polymer solution concentration in mg/ml, as determined by GIXR.

## Results And Conclusions

The thin film thickness as a function of solution concentration showed a linear relationship (Figure 1). The first round of AFM images taken of the samples as spun showed majority perpendicular cylindrical orientation for all samples but the 147.0 nm film. Perpendicular alignment looked particularly good in medium thickness samples such as the 57.1 nm and 70.5 nm samples (Figures 2 and 3). This observation undermined the hypothesis that a third component, polyisoprene, would be necessary for spontaneous perpendicular alignment.

There was no strong long-range ordering in the samples, which we determined from the lack of regular hexagonal patterning. On the other hand, initial results from the PLA-degraded samples showed more parallel cylindrical ordering in samples that appeared to have perpendicular ordering with the PLA component present. All the samples need to be further analyzed before any solid conclusions can be drawn.

## Future Work

First and foremost, the remaining PLA-degraded samples need to be further characterized. Then, the images taken will be further analyzed to determine the average feature size of the perpendicular holes (i.e. from the PLA cylinders). If PS-PLA turns out to be a viable option for pattern transfer, further work will be required to determine how to create a pattern of freestanding cylinders, i.e. degrading the majority matrix. One option is to stain the PLA with a metal, which would make it an etch resist. The group is also currently pursuing techniques to hard mask the pattern. This helps to preserve the pattern while the magnetic film is etched.

## Acknowledgements

The author would like to acknowledge and thank Dr. Marc Hillmyer and Dr. Chris Leighton for their direction and insight, Marc Rodwogin and Toshi Kubo for their knowledge and support, the National Nanotechnology Infrastructure Network Research Experience for Undergraduates Program and the NSF for funding, and the rest of the Hillmyer and Leighton groups.

## References

- [1] Zalusky, A.S.; "Mesoporous polystyrene monoliths"; *J. Chem. Soc.*, 123, 1519-1520 (2001).
- [2] Zalusky, A.S.; "Ordered nanoporous polymers from polystyrene-poly lactide block copolymers"; *J. Chem. Soc.*, 124, 12761-12773 (2002).
- [3] Mao, H.; "Control of pore hydrophilicity in ordered nanoporous polystyrene using an AB/AC block copolymer blending strategy"; *Faraday Discussions*, 128, 149-162 (2005).

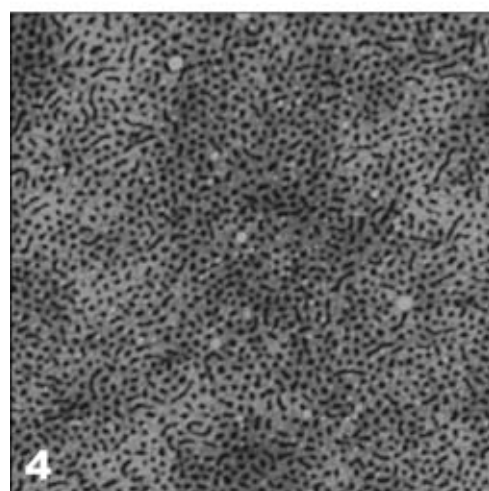
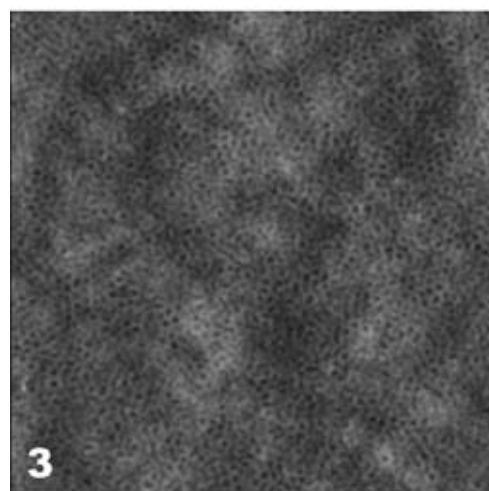
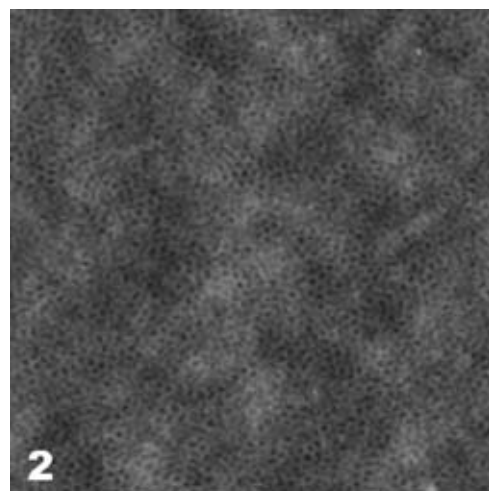


Figure 2, top: 57.1 nm thin film on Ni/FeAu substrate, as spun,  $2 \times 2 \mu\text{m}$  image.

Figure 3, middle: 70.8 nm thin film on Ni/FeAu substrate, as spun,  $2 \times 2 \mu\text{m}$  image.

Figure 4, bottom: 95.0 nm thin film on Ni/FeAu substrate, PLA degraded,  $2 \times 2 \mu\text{m}$  image.